AN EXPERIMENTALLY VERIFIED MODEL FOR THERMAL MICROACTUATORS INCLUDING NONLINEAR MATERIAL PROPERTIES, RADIATION, AND INTRA-DEVICE HEAT CONDUCTION

A Thesis

by

KEEGAN DAVID COLBERT

Submitted to the Office of Graduate and Professional Studies of
Texas A&M University
in partial fulfillment of the requirements for the degree of

MASTER OF SCIENCE

Chair of Committee,	James G. Boyd
Co-Chair of Committee,	Mohammad Naraghi
Committee Members,	Debjyoti Banerjee
Head of Department,	Rodney Bowersox

May 2016

Major Subject: Aerospace Engineering

ABSTRACT

A multi-physics model and computational method is presented for predicting the performance of thermal microactuators at high input powers. The model accounts for nonlinear temperature dependence of material properties, heat loss due to radiation, and intra-device heat transfer by conduction across an air gap. To solve the highly nonlinear governing heat equations and compute the temperature distribution in the actuator, the Galerkin method with Newton-Raphson iteration is employed, enabling the calculation of device displacement. To verify accuracy, the model is applied to the case of a flexure actuator operating at steady state, and model predictions are compared with experimental voltage, current, and displacement measurements. To investigate the effects of each nonlinearity in the model, the predictions of six additional hypothetical models are considered in which (1) intra-device heat transfer is neglected, (2) heat loss due to radiation is neglected, (3) the thermal conductivity of silicon is assumed to be temperature-independent, (4) the thermal conductivity of air is assumed to be temperature-independent, (5) the electrical resistivity of silicon is assumed to be a linear function of temperature, and (6) the thermal expansion coefficient of silicon is assumed to be temperature-independent. With the exception of heat transfer due to radiation, each source of non-linearity was shown to have a significant impact on the accuracy of model predictions at high electrical power input. The model is further applied to predict the dynamic performance of the flexure actuator using an implicit Euler method to predict the evolution of the temperature distribution over time. The dynamic implementation is then used to calculate the thermal time constant for the flexure actuator, and model predictions for the transient voltage-current response are verified experimentally.

ACKNOWLEDGMENTS

I would like to thank my committee chair, Dr. Boyd, and my committee co-chair, Dr. Naraghi, for their continued support and guidance over the course of this research. I would also like to express my gratitude to my committee member, Dr. Banerjee, for his thoughtful suggestions and advice. Their contributions have been tremendously helpful toward making this project a success. I would also like to thank my friends and family for their loving support and encouragement. I am truly grateful for all that these people have done to make this a valuable experience.

NOMENCLATURE

A	Cross-sectional area
A_{cd}	Surface area over which heat is conducted to the external environment
$A_h, A_g\ A_c, A_f, A_e, A_{Au}, A_{Si}$	Cross-sectional area of the hot arm, connector, cold arm, flexure arm, extension arm, gold Pad Metal layer of the cold arm, and silicon layer of the cold arm respectively
c	Specific heat capacity
$\boldsymbol{c}$	Set of scalar coefficients to the test functions
c_a	Specific heat capacity of air
c_{Si}	Specific heat capacity of silicon
d	Damping coefficient
E	Elastic modulus
$\boldsymbol{f}$	Flexibility matrix
$\boldsymbol{F}$	Global load vector
$\boldsymbol{F^e}$	Element load vector
$F_{h,i}, F_{g,i}, F_{c,i}, F_{f,i}$	Axial forces in the hot arm, connector, cold arm, and flexure arm respectively
F_{th}	Thermal force
g	Width of air gap
g_a	Gravitational acceleration
Gr	Grashof number
h	Thickness of device
h_{cv}	Heat transfer coefficient for convection
h_{eq}	Overall heat transfer coefficient

I_h, I_c, I_f	Moment of inertia of the hot arm, cold arm, and flexure arm respectively
I_{el}	Electric current
J	Current density
K	Boltzmann constant
$\boldsymbol{K}$	Global stiffness matrix
$\boldsymbol{K^e}$	Element stiffness matrix
k	Thermal conductivity
$k_{0Si}, k_{ia}\ \rho_{iSi}, \alpha_i, \rho_{ic}, c_{iSi}, c_{ia}$	Curve fitting parameters
k_a	Thermal conductivity of air
$k_{a,avg}$	Temperature average of the thermal conductivity of air
k_m	Mechanical stiffness of the actuator
k_{Si}	Thermal conductivity of silicon
L	Length
$L_h, L_c, L_f, L_e, L_{Au}$	Length of the hot arm, cold arm, flexure arm, extension arm, and gold Pad Metal layer respectively
m	Effective mass of the actuator
$M_{h,i}, M_{g,i}, M_{c,i}, M_{f,i}$	Moments in the hot arm, connector, cold arm, and flexure arm respectively
Nu	Nusselt number
$\boldsymbol{n}$	Unit vector normal to a boundary
n	Mesh parameter
P_∞	Ambient pressure
Pr	Prandtl number
q	Heat flux

q_{cdi}	Heat flux conducted internally
q_{cde}	Heat flux conducted to the environment
q_g	Heat flux from the actuator to the air gap
q_J	Volumetric rate of heat generation by Joule heating
q_m	Heat flux from the air gap to the actuator
q_r	Heat flux due to radiation
R	Total electrical resistance of the actuator
R_c, R_{Au}, R_{Si}	Electrical resistance of the cold arm, gold Pad Metal layer of the cold arm, and silicon layer of the cold arm respectively
R_i	Radial distance from the centroid of an arm to the arm surface
R_o	Radial distance from the centroid of an arm to the substrate
Ra	Rayleigh number
s	Coordinate from terminal of the hot arm, following the axis of each arm around the perimeter of the actuator
S_{cd}	Length of the boundary over which conduction to the environment occurs
S_f	Conduction shape factor
S_r	Length of the boundary over which radiation to the environment occurs
T	Temperature
T_∞	Ambient temperature
u	Displacement in the y-direction
u_{tip}	Displacement in the y-direction at the tip of the extension arm
V	Applied voltage across the actuator terminals
$w_h, w_c, w_f, w_e, w_{Au}$	Width of the hot arm, cold arm, flexure arm, extension arm, and gold Pad Metal layer respectively

x, y	Rectangular coordinates
$\boldsymbol{X}$	Redundant component vector
α	Thermal expansion coefficient of silicon
α_d	Thermal diffusivity of the working fluid
β	Volumetric thermal expansion coefficient of the working fluid
$\boldsymbol{\Delta}$	Displacement vector at the terminal of the hot arm
ΔL	Thermal expansion mismatch between the hot and cold sides of the flexure actuator
δM	Moment resulting from the application of a unit redundant
δ_p	Thermal penetration depth
ε	Emissivity
ϑ	Coordinate following perimeter of an arm's cross section
ξ, η	Local coordinates for the master element used in the finite element approximation
ν	Kinematic viscosity
ρ	Electrical resistivity
ρ_{Au}	Electrical resistivity of gold
ρ_{Si}	Electrical resistivity of silicon
ρ_c	Effective electrical resistivity in the cold arm
ϱ	Mass density
ϱ_{Si}	Mass density of silicon
ϱ_a	Mass density of air
σ	Stefan-Boltzmann constant
ς	Volumetric rate of heat production

τ	Thermal time constant
φ	Electrical potential
$\boldsymbol{\phi}$	Set of shape functions
χ	Error parameter
ψ	Weight function

TABLE OF CONTENTS

Page

LIST OF FIGURES

LIST OF TABLES

1. INTRODUCTION AND LITERATURE REVIEW

In recent years, micromachined devices have become widely used for applications in sensing and actuation. The use of microelectromechanical systems (MEMS) specifically for actuation has allowed for precise manipulation of micro- and nano-scale structures at relatively high frequency and with high repeatability. MEMS actuators have been used in a variety of applications, including use as microgrippers, micropumps, microvalves, and optical switches. Several mechanisms of electro-mechanical coupling have been exploited to achieve actuation, including electrostatics, the piezoelectric effect, and thermal expansion.

Electrostatic comb drives [1] are capacitive actuators composed of two combs, a stationary comb fixed to the substrate and a moveable comb mounted to the substrate via a flexible tether. The two combs are arranged such that each finger of the moveable comb is equidistant from two fingers on the stationary one. Applying a potential difference between the two combs creates an electrostatic force that causes motion in the moveable comb. Though these actuators can be operated at high frequency, displacement is often limited by the stiffness of the tether required to prevent pull-in instability.

To achieve a larger stroke, inchworm actuators have been introduced [2]. These devices consist of a long flexible strip of material mounted to two support structures. The foreword support structure is first clamped to the substrate to prevent motion while the strip is deflected, causing the aft support to move foreward. The aft support is then clamped while the foreword support is released, allowing the actuator to move incrementally along the line of action. Variations of this basic concept have also been implemented, as shown in [3].

Piezoelectric material containing polarized dipoles have also been employed as MEMS actuators. Electro-mechanical coupling in the material induces a strain when an electric potential

gradient is applied. Displacements attainable with piezoelectric material alone are relatively small, so piezoelectric actuators are usually designed in a manner that amplifies these displacements.

Thermal microactuators are widely used for their ability to reliably produce relatively large, precise displacements with high actuation force. Electro-mechanical coupling in thermal microactuators is achieved by applying an electrical potential gradient across a micromachined device, resulting in controlled nonuniform temperature changes via Joule heating. The thermal expansion caused by Joule heating can be used for actuation at the nano- and micrometer scale. Numerous designs have been proposed to achieve both in-plane and out-of-plane displacement through thermal actuation.

U-shaped flexure actuators and V-shaped bent-beam actuators are the most commonly used thermal microactuator designs for in-plane displacement [4]. Flexure actuators operate on the principal that the heat generated by an electrical current in a conductive element scales proportionally with the electrical resistance of the element. The rise in temperature therefore scales inversely with the cross-sectional area. To use this principle in flexure actuators, thick and thin elements (respectively referred to as cold and hot arms) are electrically connected in series. By arranging these two arms in a U-shape, the difference in thermal expansion creates in-plane bending. In a V-shaped bent-beam actuator, current flows across a single symmetric V-shaped beam, considered to be in a state of "pre-bending." Thermal expansion in the beam causes a central shuttle to move in the direction of the bend.

In an attempt to improve the efficiency of the flexure actuator design, modifications have been made to incorporate two hot arms, eliminating current flow in the cold arm [5]. Arrangements of both flexure actuators and bent-beam actuators have also been established to create more intricate devices, including microgrippers [6, 7] and 6-axis positioners [8]. Out-of-plane actuation can also be achieved by offsetting the hot and cold arms in the out-of-plane direction [9, 10].

The design of thermal actuators requires multi-physics models that can reliably predict the electro-thermo-mechanical response of the device. Analytical solutions have been established to predict the displacement of thermal microactuators in [5-7, 10-16]. To model the temperature distribution in a device, these analytical solutions require that significant simplifying assumptions be made. For instance, thermal conductivity in many cases is assumed to be temperature-independent and electrical resistivity is assumed to vary linearly with temperature, despite both showing a strong nonlinear temperature dependence [17]. With regards to electrical resistivity, a temperature increase in semiconductors initially corresponds with a reduction in carrier mobility, resulting in an increase in the observed electrical resistivity. However, after exceeding a critical temperature, any further increase in temperature results in a decrease in the observed electrical resistivity due to an increase in carrier concentration [18]. It is therefore important to capture this nonlinear behavior when modeling devices at high operating temperature. Analytical solutions often also assume that intra-device heat transfer and radiative heat transfer are insignificant. Intra-device heat transfer, caused by heat conducting from one location of the actuator to another through an adjacent air gap, can become quite significant when temperature gradients are large or when arms of an actuator are spaced close together. Radiative heat transfer, though insignificant at low temperatures, may become significant in a vacuum or when high input powers are required.

Attempts have been made to improve upon the accuracy of analytical models using commercially available finite element software. References [19] and [20] have established models using the commercial finite element package ANSYS, accounting for intra-device heat transfer, temperature-dependent convection, and the nonlinear temperature dependence of thermal conductivity in silicon. However, radiation was excluded from the analyses, and resistivity was assumed to be a monotonically increasing function of temperature, in contrast with the nonlinear dependence stated previously. References [9] and [21] have established ANSYS models that

consider intra-device heat transfer, temperature-dependent convection, radiative heat transfer, and the nonlinear temperature dependence of thermal conductivity in silicon. However electrical resistivity was assumed to show only linear temperature dependence. A tabulated summary of the current literature can be found in Table I.

Although the emphasis of this work is placed on applications in thermal microactuation, accurate thermal modeling is important in nearly all heat producing micromachined devices. The development of accurate electro-thermal models for large temperature ranges can help better predict the conditions that will lead to thermal runaway and device failure. Due to the cost and long lead times associated with fabrication of micromachined devices, it is not always feasible to iterate on device designs, making the establishment of accurate thermal models essential to the design process. The current work establishes a model that fully retains the temperature dependence of material properties and allows for the consideration of convection, conduction, and radiative heat transfer boundary conditions. To solve the highly nonlinear heat equation and determine the temperature distribution in the device, a computational approach that incorporates the Galerkin method with Newton-Raphson iteration is employed. This approach is then applied to a thermal flexure microactuator to determine the steady state device displacement over a wide range of input powers. The results are then verified experimentally using a flexure actuator fabricated from the SOIMUMPS micromachining process, and the significance of each nonlinearity is investigated with regards to model accuracy. The computational approach is further employed to determine the evolution of the temperature distribution over time, permitting the calculation of the dynamic device displacement and frequency response. Though measurement of device displacement is difficult at high frequencies, the model is verified experimentally by comparing the predicted voltage-current response with that measured experimentally.

TABLE I
SUMMARY OF THE LITERATURE

Reference	Device	Model type	Elastic Modulus of Active Material	Thermal Expansion Coefficient of Active Material	Thermal Conductivity of Active Material	Resistivity of Active Material	Heat Transfer Coefficient	Intra-Device Conduction	Radiation
[11]	Flexure	A	C	C	C	L	C	N	N
[22]	Flexure (electrostatic/thermal)	FE	C	F	F	C	C	N	N
[23]	Flexure	FE	C	C	C	C	C	N	N
[12]	V-shaped	A	C	C	C	L	N	N	N
[24]	Dual Flexure	FE	C	F	F	C	F	F	F
[7]	V-shaped/Flexure	A/FE/FD	C	C	C	L	C	N	N
[10]	Bi-directional out-of-plane	A/FE	C	C	C	L	C	N	N
[8]	6-axis positioner	FE	C	C	C	C	N	N	N
[25]	Unique Microgripper	FE	C	C	C	C	C	N	N
[26]	Gap Adjustable Comb (flexure)	M/NA/FE	C	L	L	L	C	N	N
[20]	Flexure	FE	C	F	F	MI	F	F	N
[27]	Flexure	FE	C	C	F	L	C	N	N
[13]	Flexure	A	C	C	C	C	C	N	N
[14]	Flexure (externally heated)	A/FE	C	C	C	n/a	C	N	N
[5]	Two Hot Arm Flexure	A/FE	C	C	C	L	C	N	N
[28]	Flexure	FE	L	F	B	L	F	F	N
[29]	Flexure	NA	C	L	L	L	C	N	N
[30]	Flexure	A/FE	C	I	I	I	C	F	N
[9]	Out-of-plane	FE	C	F	F	L	F	F	F
[21]	Flexure	FE	C	F	F	L	F	F	F
[31]	Beam	TN	C	C	C	C	C	N	N
[32]	Flexure	M/FD/FE	C	F*	C	C	C	N	N
[33]	Flexure	FE	C	F	F	L	F	F	L
[19]	Flexure	FE	C	F	F	MI	F	F	N
[34]	V-shaped	FD	C	C	F	L	F	N	F
[35]	Out-of-plane (eccentric loading)	FE	C	L	F	L	N	N	N
[15]	Dual flexure	A/FE	C	C	C	L	C	N	N
[6]	Dual flexure	A/FE	C	C	C	L	C	N	N
[36]	Flexure	FD	C	C	C	L	C	N	N
[37]	Out-of-plane	FD	C	C	F	L	C	N	F
[16]	Flexure	A	C	C	C	C	C	N	N
[38]	V-shaped	FD	C	F	F	MI	F	N	F

Summary of the current literature. (A) analytical, (C) constant, (B) minimum of two values, (F) fully accounts for temperature dependence or the given heat transfer mechanism, (F*) uses average temperature to determine the value, (FE) finite element, (FD) finite difference, (I) iterative approach, (L) linear, (M) macromodel, (MI) monotonically increasing function of temperature, (N) does not account for the corresponding mechanism, (NA) nodal analysis, (n/a) not applicable, (TN) thermal network.

Overviews of the flexure actuator design, fabrication process, and the applicable material properties are outlined in Sections 2.1 through 2.3.1. Summaries of the electro-thermal and thermo-mechanical models are then provided in Sections 2.3.2 and 2.3.3, and a computational approach used to predict the steady state behavior of the flexure actuator is discussed in Section 3.2. The predictions of this steady state model are presented in Section 3.5 along with an investigation into the significance of each source of nonlinearity in the model. In Section 4.3, the computational method is then extended to predict the dynamic performance of the flexure actuator, and the model predictions and experimental verification are presented in Section 4.5.

2. DEVICE OVERVIEW

2.1. Conceptual Design

The design of micromachined flexure actuators has been widely studied in the literature and has been selected as the test actuator for experimental verification of the presented model. As shown in Fig. 1(a), the typical flexure actuator consists of a hot arm, a cold arm, and a flexure arm. An extension arm is often placed at the tip of the actuator to amplify the displacement and has therefore been incorporated into the design of the test actuator. When an electric potential difference is applied between the hot and cold terminals, current flows through the hot arm, cold arm, and flexure arm. Because these arms are electrically connected in series, the applied voltage induces Joule heating proportional to the resistance. The resistance itself is inversely proportional to the width of the arm, resulting in greater heating of the hot arm. The larger thermal expansion of the hot arm relative to the cold arm produces a bending moment, resulting in lateral displacement of the actuator tip in the direction of the cold arm. A microscope image of this actuation is shown in Fig. 2.

For the purposes of this work, the body of air contained between the cold/flexure arm and the hot arm is referred to as the air gap. If a significant temperature gradient exists across this air gap, heat conducted between the hot and cold/flexure arm through the air gap (henceforth referred to as intra-device heat transfer) may become significant. This mechanism of heat transfer decreases the temperature of the hot arm and increases the temperature of the cold arm, ultimately decreasing the displacement of the actuator for a given electrical input. To enhance the displacement of the actuator, an electrically conductive thin film can be deposited on the surface of the cold arm. This decreases the resistivity of the arm, thus decreasing the heat generated by Joule heating. Therefore, as shown in Fig. 1(a) and (b), a gold Pad Metal layer (described in Section 2.2) was deposited on the cold arm of the test actuator and will be considered in the development of the electro-thermal

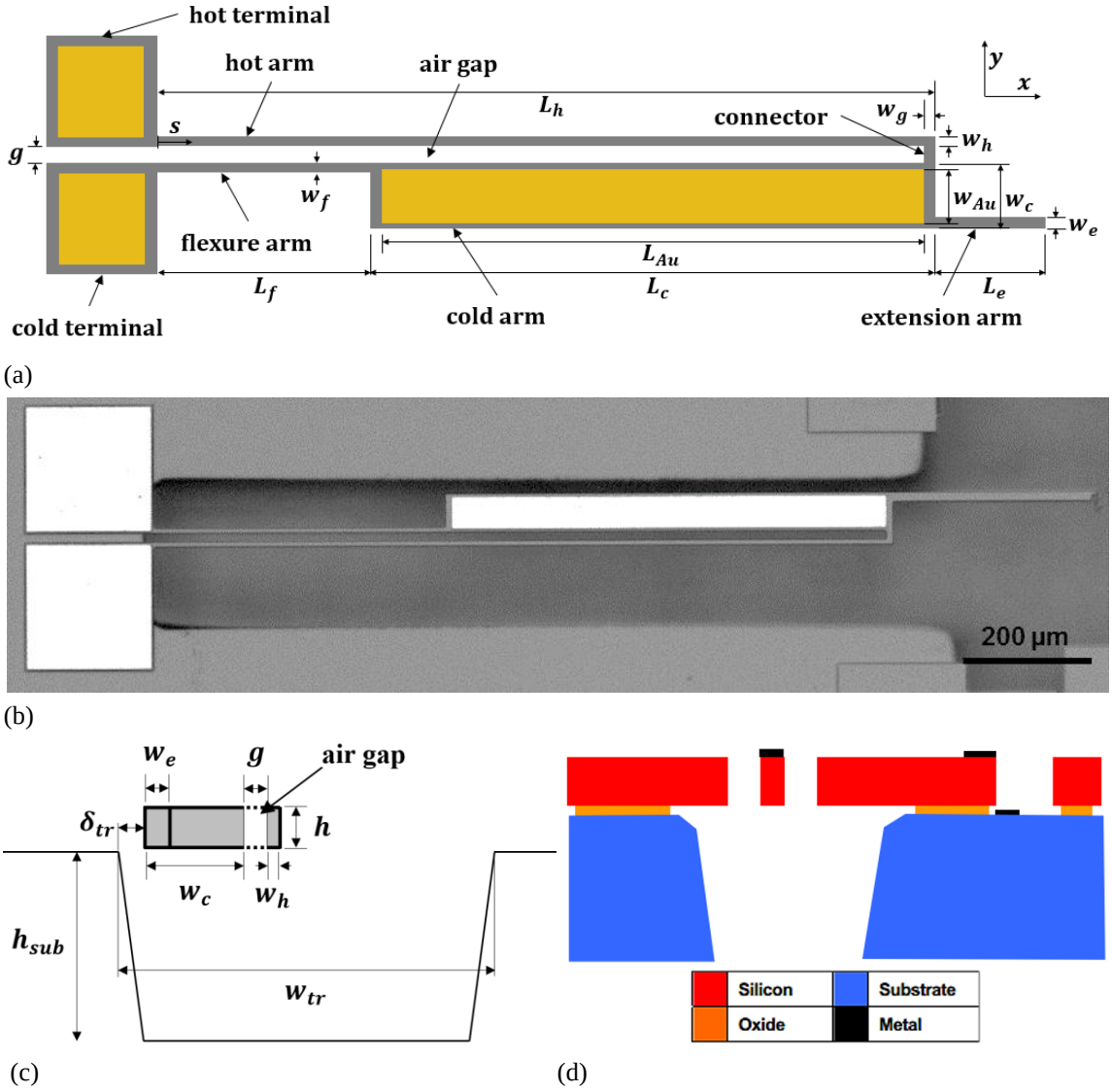

Fig. 1. (a) Flexure actuator schematic; (b) Optical microscope image of the test actuator; (c) Cross-sectional schematic of the test actuator, where boundaries across which heat is conducted to the external environment are displayed in bold; (d) Schematic of the SOIMUMPs process [39].

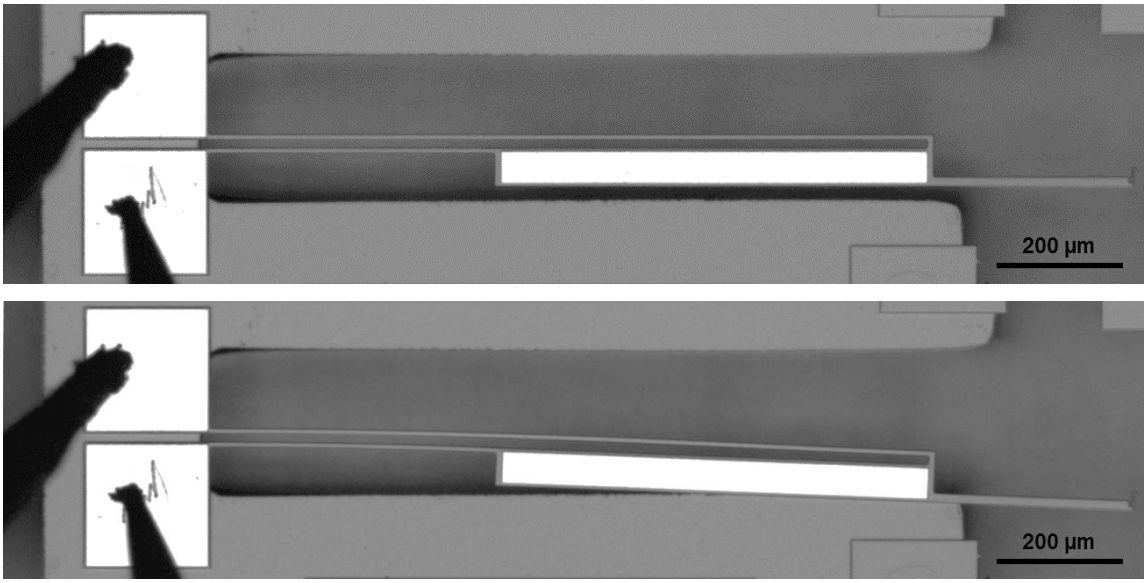

Fig. 2. Flexure actuator before actuation (top) and after actuation with a 16.5 V excitation (bottom).

model. A full list of the test actuator dimensions [corresponding with those shown in Fig. 1(a)] is given in Table II.

2.2. Device Fabrication

The test actuator, shown in Fig. 1(b), was fabricated using the SOIMUMPs Silicon-on-Insulator micromachining process. A detailed description can be found in [39], and a schematic of the process is shown in Fig. 1(d). The SOIMUMPs silicon substrate is covered with a 2 µm thick layer of oxide covered by a 25 µm thick layer of single crystal silicon. Doping of the active

TABLE II
NOMINAL TEST ACTUATOR DIMENSIONS

L_c	693.25	w_c	59.75	w_e	14.50
L_h	1145.00	w_h	7.50	w_{Au}	49.75
L_e	313.00	w_f	7.50	g	13.50
L_{Au}	673.25	w_g	10.00	h	25.00
δ_{tr}	16.00	w_{tr}	232.00	h_{sub}	400.00

Nominal dimensions for the test actuator are given in µm and correspond with the dimensions shown in Fig. 1(a). The SOIMUMPs process uses a 0.25 µm grid spacing, with a 2 µm minimum feature size.

(moveable) silicon layer is first performed by depositing a layer of phosphosilicate glass (PSG) on the frontside of the wafer and annealing at 1050°C for 1 hour. A Pad Metal layer is then patterned onto the frontside of the wafer by depositing a 20 nm layer of chrome followed by a 500 nm layer of gold. Patterning of the active silicon layer is performed using a Deep Reactive Ion Etch (DRIE) to the frontside of the wafer. A trench is then patterned into the substrate by applying a Reactive Ion Etch to the backside, followed by a wet etch to remove the exposed oxide layer. This step releases portions of the active silicon layer positioned above the trench. A final vapor HF etch is used to remove remaining oxide from the frontside.

2.3. Theoretical Modeling

Accurate modeling of the flexure actuator requires knowledge of the temperature distribution in the device. To predict this, the electro-thermo-mechanical problem is first decoupled into an electro-thermal problem and a thermo-mechanical problem. The solution to the heat balance equations governing the electro-thermal problem permits the calculation of the temperature distribution in the device, which subsequently forms the input to the thermo-mechanical problem. Using the calculated temperature distribution, thermal expansion in each arm is calculated, and the method of virtual work is applied to calculate the displacement at the tip of the extension arm.

2.3.1.Temperature Dependence of Material Properties

The temperature dependence of the thermal conductivity, thermal expansion coefficient, and electrical resistivity of silicon in the SOIMUMPS process has been investigated and reported in [17]. Although the thermal conductivity of single crystal silicon shows little doping dependence, the dopant concentration can have a significant effect on the thermal expansion coefficient and electrical resistivity. However, because the SOIMUMPs process is a standardized commercial process, the values in [17] have been assumed to be applicable to the current work. In the current model, a least squares fit was performed to establish the functional relationship between the

material properties and temperature. Equations (1), (2), (3), and (4) were determined to model the thermal conductivity of silicon, k_{Si}, the thermal conductivity of air, k_a, the electrical resistivity of silicon, ρ_{Si}, and the thermal expansion coefficient of silicon, α, sufficiently well.

$$k_{Si} = \frac{k_{0Si}}{T} \tag{1}$$

$$k_a = k_{0a} + k_{1a}T + k_{2a}T^2 \tag{2}$$

$$\rho_{Si} = \rho_{0Si} + \rho_{1Si}T + \rho_{2Si}T^2 + \rho_{3Si}T^3 + \rho_{4Si}T^4 \tag{3}$$

$$\alpha = \alpha_0 + \alpha_1 T + \alpha_2 T^2 + \alpha_3 T^3 + \alpha_4 T^4 + \alpha_5 T^5 \tag{4}$$

Here T is temperature and k_{0Si}, k_{ia}, ρ_{iSi}, and α_i are curve fitting parameters. Although these functions were used for simplicity, the model is not limited to the forms given in (1)-(4). Because the electrical resistivity of silicon is highly process-dependent, the reader is directed to [18] and [40] for physics-based analytical models should empirical data be unavailable.

The change in the elastic modulus of silicon, E, has been shown to be less than 10% in the range of 298-1273 K for Boron-doped silicon [41, 42]. Therefore, because there is limited data in the literature characterizing the temperature dependence of E for Phosphorus-doped silicon, a constant value of 169 GPa has been assumed for this work (corresponding with the <110> crystal direction) [43]. In Section 3.5.4, it will be shown that assuming E to be temperature-independent does not significantly affect the accuracy of the model.

A Pad Metal layer was deposited on the cold arm of the test actuator to decrease the effective resistivity in the arm and increase the displacement of the actuator. Therefore it is necessary to model the functional relationship between the effective resistivity in the cold arm and temperature. The cold arm is approximately modeled as two parallel temperature-dependent resistors. Hence the total resistance in the cold arm is given by

$$R_c(T) = \left[\frac{1}{R_{Si}(T)} + \frac{1}{R_{Au}(T)}\right]^{-1}. \quad (5)$$

Here R_{Si} and R_{Au} are the total resistances of the silicon and gold layer respectively, where $R(T) = \rho(T)L/A$. The parameter A is the cross-sectional area of the layer, ρ is the electrical resistivity of that layer, and L is the length of that layer. The effective resistivity can now be obtained by taking into account the resistivity of gold and silicon, ρ_{Au} and ρ_{Si} respectively, where both ρ_{Au} and ρ_{Si} can be modeled using (3). The effective resistivity of the cold arm, ρ_c, is given by

$$\rho_c(T) = \frac{A_{Au} + A_{Si}}{L_c}\left[\frac{A_{Si}}{\rho_{Si}(T)L_c} + \frac{A_{Au}}{\rho_{Au}(T)L_{Au}}\right]^{-1}, \quad (6)$$

where A_{Au} and A_{Si} are the cross-sectional areas of the gold and silicon layer respectively, and L_c and L_{Au} are the lengths of the cold arm and gold layer respectively. For consistency and simplicity, a least squares fit was performed on the values given by (6) to give $\rho_c(T)$ the same form as (3). Equation (7), in which function parameters are designated ρ_{ic}, will therefore replace (3) henceforth when considering the electrical resistivity of the cold arm. A list of the material properties and function parameters used in the implementation of the presented model is given in Table III.

TABLE III
MATERIAL PROPERTIES AND FUNCTION PARAMETERS

α_0 (K^{-1})	α_1 (K^{-2})	α_2 (K^{-3})	α_3 (K^{-4})	α_4 (K^{-5})	α_5 (K^{-6})
-2.12×10^{-6}	2.62×10^{-8}	-4.65×10^{-11}	4.27×10^{-14}	-1.96×10^{-17}	3.59×10^{-21}
k_{0a} (W·m^{-1}·K^{-1})	k_{1a} (W·m^{-1}·K^{-2})	k_{2a} (W·m^{-1}·K^{-3})	k_{0Si} (W·m^{-1})	ε	E (GPa)
4.76×10^{-3}	7.81×10^{-5}	-1.53×10^{-8}	40166.3	0.7	169
ρ_{0Si} (Ω·m)	ρ_{1Si} (Ω·m·K^{-1})	ρ_{2Si} (Ω·m·K^{-2})	ρ_{3Si} (Ω·m·K^{-3})	ρ_{4Si} (Ω·m·K^{-4})	
2.64×10^{-4}	-1.38×10^{-6}	4.36×10^{-9}	-4.13×10^{-12}	1.19×10^{-15}	
ρ_{0c} (Ω·m)	ρ_{1c} (Ω·m·K^{-1})	ρ_{2c} (Ω·m·K^{-2})	ρ_{3c} (Ω·m·K^{-3})	ρ_{4c} (Ω·m·K^{-4})	
2.02×10^{-8}	4.10×10^{-9}	8.23×10^{-13}	6.16×10^{-16}	-3.44×10^{-19}	

Function parameters for α, k_{Si}, and ρ_{Si} were established from data reported in [17], E was obtained from [43], function parameters for $k_a$were obtained from data reported in [44], and function parameters for ρ_c were calculated using resistivity data for gold reported in [45].

$$\rho_c = \rho_{0c} + \rho_{1c}T + \rho_{2c}T^2 + \rho_{3c}T^3 + \rho_{4c}T^4 \tag{7}$$

To model the dynamic performance of the thermal microactuator, the temperature dependence of the specific heat capacity of silicon, c_{Si}, the specific heat capacity of air, c_a, and the mass density of air, ϱ_a, must also be considered. The following functional relationships were found to model these temperature dependences sufficiently well:

$$c_{Si} = c_{0Si} + c_{1Si}T + c_{2Si}T^2 \tag{8}$$

$$c_a = c_{0a} + c_{1a}T + c_{2a}T^2 \tag{9}$$

$$\varrho_a = \frac{P_\infty}{RT}, \tag{10}$$

where c_{iSi} and c_{ia} are function parameters, P_∞ is the ambient air pressure, and R is the specific gas constant for air. For all calculations that follow, atmospheric conditions at sea level will be assumed where P_∞ = 101 325 Pa, and R = 287.058 J·kg^{-1}·K^{-1}. A summary of these material properties and function parameters used in the dynamic implementation of the model is shown in Table IV. Here mass density of silicon, ϱ_{Si}, is assumed to be temperature-independent.

TABLE IV
MATERIAL PROPERTIES AND FUNCTION PARAMETERS FOR DYNAMIC IMPLEMENTATION OF THE MODEL

c_{0Si} (J·kg^{-1}·K^{-1})	c_{1Si} (J·kg^{-1}·K^{-2})	c_{2Si} (J·kg^{-1}·K^{-3})
5.95×10^{2}	5.38×10^{-1}	-1.77×10^{-4}
c_{0a} (J·kg^{-1}·K^{-1})	**c_{1a} (J·kg^{-1}·K^{-2})**	**c_{2a} (J·kg^{-1}·K^{-3})**
9.53×10^{2}	1.50×10^{-1}	3.03×10^{-5}
ϱ_{Si} (kg·m^{-3})	**P_∞ (Pa)**	**R (J·kg^{-1}·K^{-1})**
2329.6	101 325	287.058

Function parameters for c_{Si} were obtained from data reported in [46] and function parameters for c_a were obtained from data reported in [47].

2.3.2.Electro-Thermal Model

To reliably predict the displacement induced by thermal actuation, the temperature distribution in the actuator must be accurately described. The mechanisms of heat transfer will first be formulated pointwise in a manner that is applicable to both the actuator arms and the air gap, assuming temperature to be uniform in the out-of-plane direction. The temperature will also be assumed uniform over the cross section of each actuator arm, thus permitting the formulation of a 1-D governing differential equation for the actuator arms and a 2-D governing differential equation for the air gap. After the governing differential equations are developed, the Galerkin method with Newton-Raphson iteration will be applied to solve for the temperature distribution in the actuator (see Section 3 and 4 for the implementation of the computational method).

The heat balance equation is written as:

$$\varrho c \frac{\partial T}{\partial t} = -\boldsymbol{\nabla} \cdot q + \varsigma, \tag{11}$$

where ϱ is mass density, c is specific heat capacity, t is time, q is the heat flux entering a point, and ς is volumetric rate of heat production. The term ς is equal to zero within the air gap and equal to the heat generated by Joule heating, q_J, within the actuator. Equation (11) will now be developed for the actuator arms and air gap to account for radiation, conduction, and convection boundary conditions. Towards this end, we first consider the non-dimensional numbers commonly used to evaluate the relative importance of natural convection and conduction in the surrounding medium. The Nusselt number provides the ratio of the convective heat transfer to the conductive heat transfer and is given by $Nu = h_{cv}L/k$ where h_{cv} is the heat transfer coefficient for convection and k is the thermal conductivity of the working fluid. The test actuator has a Nusselt number on the order of 10^{-3} to 10^{-2}, assuming the heat transfer coefficient of natural convection in air to be in the range of 10-100 $W{\cdot}m^{-2}{\cdot}K^{-1}$. The Grashof number provides a ratio of buoyant forces to viscous

forces and is used to determine the significance of natural convection. A small value indicates that viscous forces dominate, and air flow is therefore limited. The Grashof number is given by $Gr = g_a\beta(T - T_\infty)L^3/\nu^2$ where g_a is the gravitational acceleration, β is the volumetric thermal expansion coefficient of the fluid, L is the characteristic length, and ν is the kinematic viscosity of the fluid [48]. For the actuator in this work, the Grashof number is on the order of 10^{-4}, suggesting that the effects of natural convection are small.

The Prandtl number provides the ratio of momentum diffusivity to thermal diffusivity and is given by $Pr = \nu/\alpha_d$, where α_d is the thermal diffusivity of the fluid. The Rayleigh number, Ra, is the product of the Prandtl number and the Grashof number, and, when lower than 1708 for air, the effects of convection can be considered negligible relative to conduction [49]. For the actuator in this work, the Rayleigh number is on the order of 10^{-5} to 10^{-4}. This provides sufficient evidence to justify neglecting convection in favor of conduction to the external environment.

It is now necessary to model the mechanisms of heat transfer and heat generation within the actuator and air gap. Properties are assumed uniform in the out-of-plane direction, and temperature is, therefore, only considered to be a function of position, (x,y), and time, t. The volumetric rate of heat production within the actuator can now be expressed as the heat generated by Joule heating:

$$q_J = \frac{1}{\rho(T)}\nabla\varphi(x,y,t)\cdot\nabla\varphi(x,y,t), \tag{12}$$

where ρ is the electrical resistivity of the semiconductor/conductor, and φ is the electrical potential. In semiconductors ρ is a strong function of doping concentration and temperature. For a given micro-scale device, however, the area of the die covered by the device is generally small enough that the doping concentration can be assumed uniform. Therefore for a given doping, the resistivity can be assumed to be a function of temperature only. The heat flux conducted internally can now be written in the following general form for both the air gap and the actuator:

$$q_{cdi} = -k(T)\boldsymbol{\nabla}T(x,y,t), \tag{13}$$

where k is the thermal conductivity of either the air or the actuator material. Because this thermal model is intended to predict the behavior of thermal microactuators at high operating temperatures, the effects of radiation will also be considered for the arms of the actuator. The heat flux due to radiation, q_r, is given by

$$q_r = \varepsilon\sigma\left[T(x,y,t)|_{\partial a}{}^4 - T_\infty^4\right], \tag{14}$$

where ε is the emissivity of the semiconductor/conductor, σ is the Stefan-Boltzmann constant, T_∞ is the temperature of the ambient environment, and $T(x,y,t)|_{\partial a}$ denotes the temperature evaluated on the surface of the actuator exposed the external environment. Any boundaries between the microactuator and the air gap are not included in ∂a. Because thermal microactuators often do not operate in a vacuum, the heat flux due conduction to the external environment, q_{cde}, must also be considered. This can be written in the general form

$$q_{cde} = -[k_a(T)\boldsymbol{\nabla}T|_{\partial a}] \cdot \boldsymbol{n}|_{\partial a}, \tag{15}$$

where k_a is the thermal conductivity of air and $\boldsymbol{n}$ is the unit vector normal to the boundary. To simplify the analysis, this term will be reformulated in terms of a temperature-dependent effective heat transfer coefficient and applied to both the actuator arms and the air gap. An isothermal arm will now be considered, and the spatial dependence of temperature will temporarily be excluded. The rate of heat transfer due to conduction to the external environment, Q_{cde}, can be written in terms of a conduction shape factor, S_f, as

$$Q_{cde} = \left[\frac{1}{T-T_\infty}\int_{T_\infty}^{T} k_a(T)dT\right] S_f[T - T_\infty] = k_{a,avg}S_f[T - T_\infty]. \tag{16}$$

The term $k_{a,avg}$ is the result of taking a temperature average of the thermal conductivity of air [50]. The rate of heat transfer is given by the product of a flux and an area. The shape factor is

therefore given by an area through which heat is conducted divided by a length across which the temperature gradient is calculated. The term Q_{cde} can also be written in the following form:

$$Q_{cde} = h_{eq}(T)A_{cd}[T - T_{\infty}], \tag{17}$$

where h_{eq} is the effective heat transfer coefficient for conduction and A_{cd} is the surface area of the arm over which heat is conducted to the external environment. This area excludes that over which heat is exchanged between the arms through the air gap. The temperature-dependent effective heat transfer coefficient can now be written as

$$h_{eq}(T) = \frac{S_f}{A_{cd}}\left[\frac{1}{T-T_{\infty}}\int_{T_{\infty}}^{T} k_a(T)\, dT\right] = \frac{S_f k_{a,avg}}{A_{cd}}. \tag{18}$$

This form of h_{eq} can now be applied pointwise, yielding the following form for q_{cde}:

$$q_{cde} = h_{eq}(T)[T(x,y,t)|_{\partial a} - T_{\infty}]. \tag{19}$$

The arms of the microactuator are sufficiently slender such that the temperature variation within each cross section can be considered negligible relative to temperature variation along the length of each arm. A coordinate, s, is therefore introduced to represent the axial distance from the terminal of the hot arm, following the axis of each arm around the actuator, as shown in Fig. 1. Temperature can now be considered a function of only s within the actuator. Furthermore, the Joule heating term can be rewritten in terms of the current density, J, where $J = \boldsymbol{\nabla}\varphi/\rho$. Due to the conservation of charge principle and because the arms of the actuator have different cross-sectional areas, the current density is a piecewise constant function in s. Furthermore, a unique shape factor is considered for each arm such that the function for $h_{eq}(T)$ is also considered piecewise in s. Combining all mechanisms of heat transfer given in (12), (13), (14), and (19), the differential equation describing the heat transfer in each arm can be expressed as

$$-\varrho_{Si}c_{Si}(T)A\frac{\partial T(s,t)}{\partial t}+\frac{\partial}{\partial s}\left[k_{Si}(T)A\frac{\partial T(s,t)}{\partial s}\right]+J(t)^2\rho(T)A \\ -h_{eq}(T)S_{cd}[T(s,t)-T_\infty]-\varepsilon\sigma S_r[T(s,t)^4-T_\infty^4]-hq_g(s,t)=0, \tag{20}$$

where ϱ_{Si} is the mass density of silicon, c_{Si} is the specific heat of silicon, k_{Si} is the thermal conductivity of silicon, A is the cross-sectional area of the actuator arm, h is the thickness of the actuator, q_g is the heat flux into the air gap, S_{cd} is the length of the boundary over which conduction to the environment occurs, and S_r is the length of the boundary over which radiation to the environment occurs. S_{cd} and S_r for each arm are given by the portion of its cross-sectional perimeter illustrated with a bold line in Fig. 1 (c).

For the air gap, the temperature can be considered to be uniform in the out-of-plane direction but spatially varying in the x-y plane. Using (13) and (19), the differential equation describing heat transfer within the air gap can be expressed as

$$-\varrho_a(T)c_a(T)h\frac{\partial T(x,y,t)}{\partial t}+\boldsymbol{\nabla}\cdot[k_a(T)h\boldsymbol{\nabla}T(x,y,t)] \\ -h_{eq}(T)S_{cd}[T(x,y,t)-T_\infty]-hq_m(x,y,t)|_{\partial m}=0, \tag{21}$$

where ϱ_a is the mass density of air, c_a is the specific heat of air, and $q_m|_{\partial m}$ is the heat flux into the microactuator evaluated on the boundary. In (21), the value of S_{cd} is 2, corresponding to the top and bottom surfaces of the actuator. In the formulation of the governing differential equations, q_g and q_m have been introduced to represent intra-device heat transfer. However, in the solution method presented, both gap elements and actuator elements will be included within a single model. The spatial coupling of (20) and (21) will therefore be captured by the common nodes shared between actuator elements and air gap elements, and intra-device heat transfer will inherently be considered. The terms q_g and q_m have only been added for illustrative purposes and will be dropped from the equation when applying the Galerkin method. Furthermore, both (20) and (21)

will be considered independent of the mechanical behavior of the device such that the electro-thermal and thermo-mechanical responses can be solved sequentially.

Determining the effective heat transfer coefficient to be used in (19) first requires calculation of the conduction shape factor for each arm. Due to the rather complicated geometry of the device being analyzed in this problem, closed-form solutions for these shape factors are not available. To minimize the computational cost associated with running an additional finite element analysis, a method is proposed to establish an equivalent system for which there exists an analytical solution for the conduction shape factor.

For the purposes of this calculation, a two dimensional cross section of each arm is examined, as shown in Fig. 3. It will be assumed that all heat is conducted radially outward from the centroid of the cross section and reaches ambient temperature at the substrate. Therefore, heat conduction can be approximately modeled as

$$\frac{Q_{cde}}{ds} = k_{a,avg} \oint \frac{[T(s) - T_\infty]}{\Delta R}\, d\vartheta, \tag{22}$$

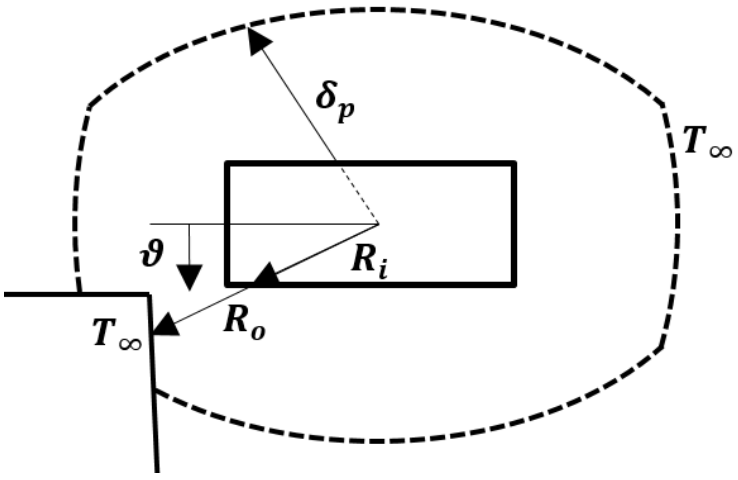

Fig. 3. Cross-sectional schematic for calculating the conduction shape factor.

where ϑ is the dimension along the perimeter of the arm's cross section, representing the area over which heat is conducted to the external environment per unit length of the arm. As shown in (23), ΔR represents the smaller of two quantities: either the radial distance from the external surface of the arm to the substrate or the thermal penetration depth, δ_p. The thermal penetration depth represents the depth at which the surrounding medium reaches ambient temperature, and it can be approximated using (24) [48]. Hence (22) replaces the shape factor [shown in (16)] with the area over which heat is conducted divided by the distance required for temperature to drop from T to T_∞. As mentioned previously, heat transfer between arms through the air gap will inherently be considered in the implementation of the computational method, and thus it is not to be included in the calculation of this heat transfer coefficient. Therefore any boundaries between the air gap and the microactuator arms are not included in the boundary integral.

$$\Delta R = \min\left(R_o - R_i, \delta_p\right) \tag{23}$$

$$\delta_p = \sqrt{\tau \alpha_d} \tag{24}$$

In (23), R_i is the radial distance from the centroid of the arm to the surface of the arm, and R_o is the radial distance from the centroid of the arm to the surface of the substrate. The thermal time constant, τ, is the time required for the actuator to reach a state of equilibrium with the environment. For thermal microactuators, τ generally ranges from 0.5-1.0 ms [51]. If the thermal diffusivity of air at 298 K is assumed, this leads to a penetration depth ranging from 105 μm to 149 μm. Therefore in the implementation of the steady state model, this range of penetration depths will be used as an initial approximation. As will be shown in Section 4, however, the implementation of the dynamic model will permit the approximation of the thermal time constant and, therefore, the thermal penetration depth.

In order to calculate a conduction shape factor to describe heat loss to the environment, we will consider a simpler geometry that is approximately equivalent to the actuator geometry in terms of heat transfer. The use of this simpler geometry permits the utilization of closed-form solutions already developed in literature. To this end, an isothermal cylinder (representing the actuator arm) is considered with radius, r_i, such that the surface area of the cylinder is equal to the surface area of the actuator arm. A larger concentric cylinder with an isothermal surface (representing the depth at which temperature reaches that of the ambient environment) and radius r_o is then considered such that $\oint d\vartheta/\Delta R$ is the same for both cases, resulting in comparable heat flow:

$$\frac{2\pi r_i}{r_o - r_i} = \oint \frac{d\vartheta}{\Delta R}. \tag{25}$$

The left hand side of (25) is $\oint d\vartheta/\Delta R$ evaluated for the equivalent cylinder geometry in which heat flows from the surface of the smaller cylinder to the surface of the larger cylinder. This is set equal to the same integral evaluated for the actuator geometry shown in Fig. 3. By satisfying (25), a given temperature difference, ΔT, will result in approximately the same heat flow per unit length of the arm for both geometries. From (25), r_o can be calculated. With this approximation, a complicated geometry with no explicit analytical shape factor can be converted into an approximately equivalent geometry with a known closed-form solution for the shape factor. The shape factor for this equivalent configuration is given by

$$S_f = \frac{2\pi L}{\ln\left(\frac{r_o}{r_i}\right)}, \tag{26}$$

where L is the length of the arm [50]. Equations (26) and (2) are then substituted into (18) to yield the temperature-dependent heat transfer coefficient for each arm.

$$h_{eq}(T) = \frac{2\pi}{S_{cd} \ln\left(\frac{r_0}{r_i}\right)} \frac{1}{T - T_\infty} \left[k_{0a}[T - T_\infty] + \frac{k_{1a}[\,T^2 - T_\infty^2]}{2} + \frac{k_{2a}[T^3 - T_\infty^3]}{3} \right] \quad (27)$$

This process for calculating $h_{eq}(T)$ is performed individually for each arm of the actuator. Conduction to the environment is also considered from the top and bottom surfaces of the air gap, requiring a shape factor to be calculated for this region as well.

Given a known temperature distribution, the electrical properties of the actuator can be calculated. The total resistance, R, is found by integrating the resistance over the length of the actuator, given by:

$$R = \int_0^{L_h} \frac{\rho_{Si}(T)}{A_h}\, ds + \int_{L_h}^{L_h+g} \frac{\rho_{Si}(T)}{A_g}\, ds + \int_{L_h+g}^{L_h+g+L_c} \frac{\rho_c(T)}{A_c}\, ds + \int_{L_h+g+L_c}^{2L_h+g} \frac{\rho_{Si}(T)}{A_f}\, ds, \quad (28)$$

where A_h, A_g, A_c, and A_f are the cross-sectional areas of the hot arm, connector, cold arm, and flexure arm respectively, and L_h, g, and L_c are the lengths of the hot arm, connector, and cold arm respectively. Furthermore, once the resistance is known, the applied voltage, V, and the electrical current, I_{el}, can be related using

$$V = I_{el} R. \quad (29)$$

2.3.3.Thermo-Mechanical Model

The method used to model the deflection of the flexure actuator is largely the same as that outlined in [11]. In this analysis, the thickness of the gold layer on the cold arm is sufficiently thin such that its contribution to the mechanical properties of the device are assumed negligible. Given a known temperature distribution, the relative thermal expansion in the hot arm is first calculated with respect to the cold arm and flexure arm. The mechanical boundary conditions are then removed at the terminal of the hot arm and replaced with redundant loads, allowing the reaction forces required to enforce the displacement- and rotation-free boundary conditions to be calculated

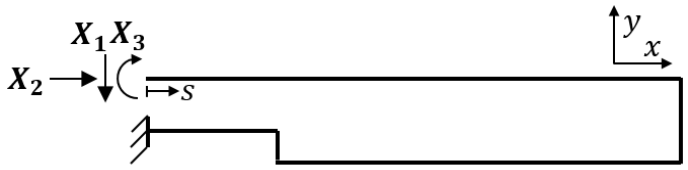

Fig. 4. Mechanical modeling of the flexure actuator as an indeterminate rigid frame.

using the method of virtual work. The method presented herein deviates slightly from [11] in that the following method considers axial deformation of each arm and calculates the moment in each arm about its centroid.

The flexure actuator is considered to be an indeterminate frame with arms fixed at the terminals. The degree of indeterminacy in this problem is 3. Therefore to calculate the deflection, the support at the terminal of the hot arm is removed and replaced with three redundant forces and moments (shown in Fig. 4): a force in the negative *y*-direction X_1, a force in the *x*-direction X_2, and a rotational moment about the negative *z*-axis X_3. The moment in each arm resulting from the application of the three redundant loads are as follows:

$$\begin{aligned}
&M_{h,1} = X_1 s && M_{h,2} = 0 && M_{h,3} = -X_3 \\
&M_{g,1} = X_1\left[L_h - \frac{w_g}{2}\right] && M_{g,2} = -X_2\left[s - L_h + \frac{w_h}{2}\right] && M_{g,3} = -X_3 \\
&M_{c,1} = X_1[2L_h + g - s] && M_{c,2} = -X_2\left[g + \frac{w_h}{2} + \frac{w_c}{2}\right] && M_{c,3} = -X_3 \\
&M_{f,1} = X_1[2L_h + g - s] && M_{f,2} = -X_2\left[g + \frac{w_h}{2} + \frac{w_f}{2}\right] && M_{f,3} = -X_3,
\end{aligned} \tag{30}$$

where w_h, w_g, w_c, and w_f are the widths of the hot arm, connector, cold arm, and flexure arm respectively. The terms $M_{h,i}, M_{g,i}, M_{c,i}$, and $M_{f,i}$ represent the moments in the hot arm, connector, cold arm, and flexure arm respectively, resulting from the application of the i^{th} redundant.

Similarly the axial force in each arm resulting from the application of the three redundant loads are as follows:

$$\begin{aligned} F_{h,1} &= 0 & F_{h,2} &= -X_2 & F_{h,3} &= 0 \\ F_{g,1} &= -X_1 & F_{g,3} &= 0 & F_{g,2} &= 0 \\ F_{c,1} &= 0 & F_{c,2} &= X_2 & F_{c,3} &= 0 \\ F_{f,1} &= 0 & F_{f,2} &= X_2 & F_{f,3} &= 0, \end{aligned} \tag{31}$$

where $F_{h,i}, F_{g,i}, F_{c,i}$, and $F_{f,i}$ are the axial forces in the hot arm, connector, cold arm, and flexure arm respectively, resulting from the application of the i^{th} redundant. Equating internal and external virtual work yields

$$\begin{aligned} \Delta_i = &\int_0^{L_h} \left[\delta M_{h,i} \frac{\sum M_{h,j}}{E(T) I_h} + \delta F_{h,i} \frac{\sum F_{h,j}}{E(T) A_h} \right] ds \\ &+ \int_{L_h}^{L_h+g} \left[\delta M_{g,i} \frac{\sum M_{g,j}}{E(T) I_g} + \delta F_{g,i} \frac{\sum F_{g,j}}{E(T) A_g} \right] ds \\ &+ \int_{L_h+g}^{L_h+g+L_c} \left[\delta M_{c,i} \frac{\sum M_{c,j}}{E(T) I_c} + \delta F_{c,i} \frac{\sum F_{c,j}}{E(T) A_c} \right] ds \\ &+ \int_{L_h+g+L_c}^{2L_h+g} \left[\delta M_{f,i} \frac{\sum M_{f,j}}{E(T) I_f} + \delta F_{f,i} \frac{\sum F_{f,j}}{E(T) A_f} \right] ds, \end{aligned} \tag{32}$$

where δM is the moment in the arm resulting from the application of a virtual load, Δ_i is the displacement vector at the removed support, E is the elastic modulus in the arm, and I is the moment of inertia about the out-of-plane axis. The redundant components can be factored out of the expression, leading to the following simple algebraic equation relating the value of the redundant components to the displacement at the removed support:

$$\Delta_i = f_{ij} X_j. \tag{33}$$

From (32) and (33), the flexibility matrix f_{ij} can be expressed as

$$\begin{aligned} f_{ij} = & \int_0^{L_h} \left[\delta M_{h,i} \frac{\delta M_{h,j}}{E(T) I_h} + \delta F_{h,i} \frac{\delta F_{h,j}}{E(T) A_h} \right] ds \\ & + \int_{L_h}^{L_h+g} \left[\delta M_{g,i} \frac{\delta M_{g,j}}{E(T) I_g} + \delta F_{g,i} \frac{\delta F_{g,j}}{E(T) A_g} \right] ds \\ & + \int_{L_h+g}^{L_h+g+L_c} \left[\delta M_{c,i} \frac{\delta M_{c,j}}{E(T) I_c} + \delta F_{c,i} \frac{\delta F_{c,j}}{E(T) A_c} \right] ds \\ & + \int_{L_h+g+L_c}^{2L_h+g} \left[\delta M_{f,i} \frac{\delta M_{f,j}}{E(T) I_f} + \delta F_{f,i} \frac{\delta F_{f,j}}{E(T) A_f} \right] ds. \end{aligned} \tag{34}$$

Assuming E to be temperature-independent, the terms of the flexibility matrix evaluate to:

$$f_{11} = \frac{L_h^3}{3EI_h} + \frac{[L_h - L_c]^3}{3EI_h} + \frac{L_h^2 L_c}{EI_c} - \frac{L_h L_c^2}{EI_c} + \frac{L_c^3}{3EI_c} + g \left[\frac{1}{A_g E} + \frac{\left[L_h - \frac{\mathrm{w_g}}{2} \right]^2}{EI_g} \right]$$

$$\begin{aligned} f_{12} = f_{21} = & -\frac{[L_h - L_c]^2 [g + w_h]}{2EI_h} - \frac{g[2L_h - w_g][g + w_h]}{4EI_g} \\ & - \frac{[2L_h - L_c] L_c [2g + w_c + w_h]}{4EI_c} \end{aligned} \tag{35}$$

$$f_{13} = f_{31} = -\frac{L_h^2}{EI_h} - \frac{L_h L_c}{EI_c} + \frac{L_h L_c}{EI_h} + \frac{L_c^2}{2EI_c} - \frac{L_c^2}{2EI_h} - \frac{g \left[L_h - \frac{w_g}{2} \right]}{EI_g}$$

$$f_{22} = \frac{L_h}{A_h E} + [L_h - L_c]\left[\frac{1}{A_f E} + \frac{[-g - w_h]^2}{EI_h}\right]$$

$$+ L_c\left[\frac{1}{A_c E} + \frac{\left[-g - \frac{w_c}{2} - \frac{w_h}{2}\right]^2}{EI_c}\right] + \frac{g\left[4g^2 + 6gw_h + 3w_h^2\right]}{12EI_g}$$

$$f_{23} = f_{32} = \frac{g^2}{2EI_g} - \frac{[L_h - L_c][-g - w_h]}{EI_h} - \frac{L_c\left[-g - \frac{w_c}{2} - \frac{w_h}{2}\right]}{EI_c} + \frac{gw_h}{2EI_g}$$

$$f_{33} = \frac{g}{EI_g} + \frac{L_h}{EI_h} + \frac{L_h - L_c}{EI_h} + \frac{L_c}{EI_c}.$$

The displacement vector, Δ_i, is considered to be known, provided that the temperature field in the actuator is known. The vector components are the displacements/rotation that must be applied to the removed support to enforce the mechanical boundary conditions of the indeterminate frame. Δ_i can be determined by evaluating the thermal expansion mismatch between the hot and cold sides of the actuator:

$$\Delta_i = \begin{vmatrix} 0 \\ \Delta L \\ 0 \end{vmatrix}, \tag{36}$$

where

$$\Delta L = \Delta L_h - \Delta L_c - \Delta L_f = \int_0^{L_h} \alpha(T)[T(s) - T_\infty]\, ds$$
$$- \int_{L_h+g}^{L_h+g+L_c} \alpha(T)[T(s) - T_\infty]\, ds - \int_{L_h+g+L_c}^{2L_h+g} \alpha(T)[T(s) - T_\infty]\, ds. \tag{37}$$

Equation (33) can then be used to solve for the values of the redundant loads, which represent the reaction forces at the terminal of the hot arm. Given the reaction forces and assuming the elastic

modulus to be temperature-independent, Euler Bernoulli beam theory can be employed to calculate the displacement at the tip of the actuator, $u(L_h)$, as follows:

$$M_h(s) = -EI_h \frac{d^2u(s)}{ds^2} = [-X_1 s + X_3] \tag{38}$$

$$u(L_h) = \frac{\left[L_h^3 X_1 - 3L_h^2 X_3\right]}{6EI_h}. \tag{39}$$

The displacement at the tip of the extension arm can also be determined by evaluating the displacement and rotation at the tip of the hot arm and extrapolating over the length of the extension arm. The displacement at the tip of the extension arm is therefore given by

$$u_{tip} = \frac{\left[L_h^3 X_1 - 3L_h^2 X_3\right]}{6EI_h} + L_e \frac{L_h^2 X_1 - 2L_h X_3}{2EI_h}. \tag{40}$$

2.3.4.Validation of the Mechanical Model

The test actuator was modeled in ABAQUS to provide finite element analysis (FEA) validation of the mechanical model presented in the previous section. A zero displacement/rotation boundary condition was enforced in all directions at the terminal face of the flexure arm, while a zero displacement/rotation boundary condition was enforced in all directions except for an applied displacement in the x-direction at the terminal face of the hot arm. The actuator was meshed with 20 node three-dimensional brick elements with reduced integration (designated C3D20R in ABAQUS) as shown in Fig. 5.

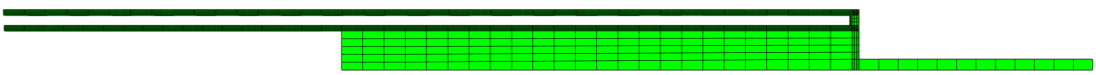

Fig. 5. Finite element mesh used for validation of the mechanical model.

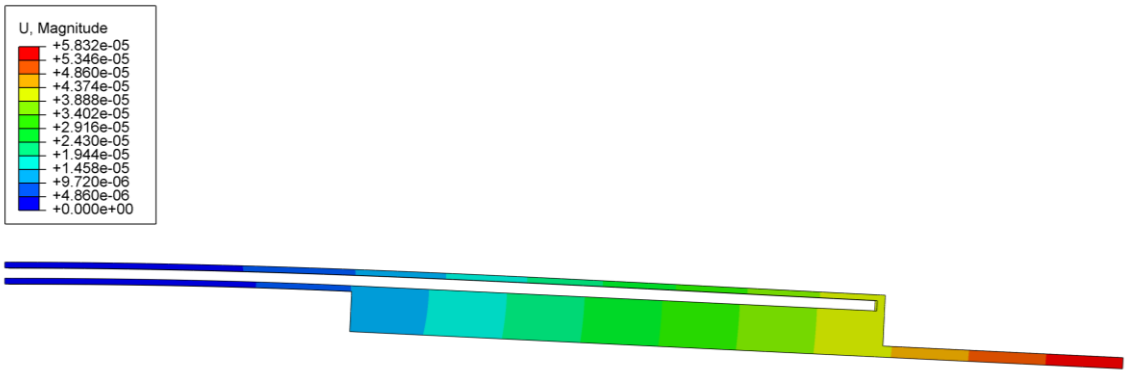

Fig. 6. Deformation of the actuator, where $\Delta L = 1.1$ µm. Contours correspond with displacement in m.

Several *x*-displacements corresponding with different values of ΔL were applied to the terminal face of the hot arm, and the resulting displacements at the tip of the extension arm were compared with the predictions of the mechanical model. Fig. 6 illustrates the deformed actuator after applying the displacement/rotation boundary conditions corresponding with $\Delta L = 1.1$ µm. Results comparing FEA to the mechanical model are displayed in Fig. 7. As shown, the mechanical model predictions exhibit good agreement with those of the finite element model.

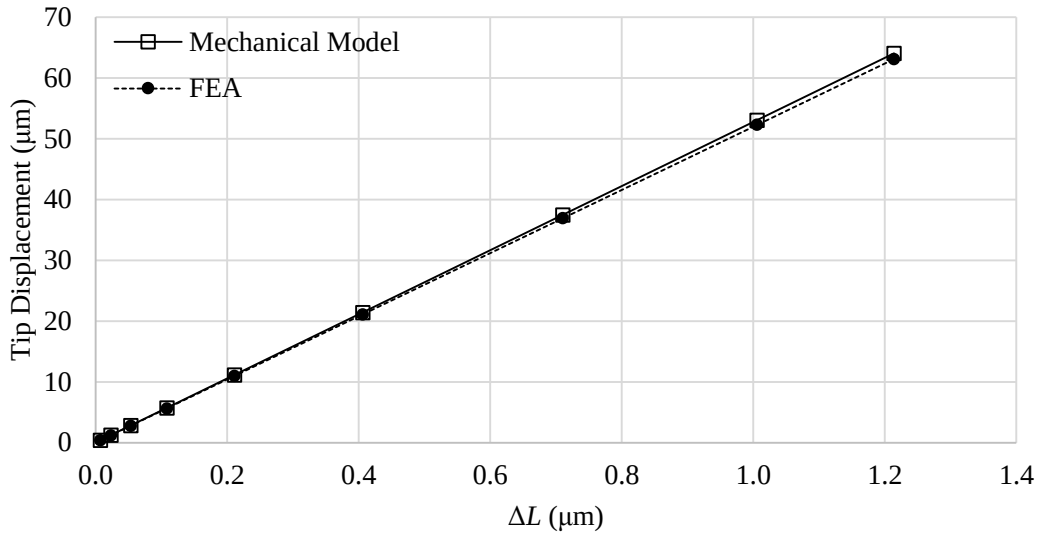

Fig. 7. Finite element validation of the mechanical model. The above plot illustrates the predicted displacement at the tip of the extension arm for different values of ΔL.

3. STEADY STATE MODELING

3.1. Introduction

As stated previously, accurate prediction of the electro-thermo-mechanical response of thermal microactuators requires the solution of multi-physics models that properly retain the physics of the problem. As illustrated in Table I, full consideration of the nonlinearities in the governing heat balance equations has yet to be carried out in the literature. The goal of this section is to outline a computational method for the implementation of the electro-thermal model presented in Section 2.3.2, assuming steady state operating conditions. The resulting temperature distribution is then used as the input to the thermo-mechanical problem presented in Section 2.3.3, from which the steady state extension arm tip displacement of the actuator can be calculated. In addition to the full thermal microactuator model that retains all mechanisms of heat transfer and the temperature dependences of material properties, several hypothetical models are introduced in which simplifying assumptions are made with regards to the nonlinearities in the model. Through comparison with experimental measurements and the predictions of the full thermal microactuator model, the significance of these sources of nonlinearity are evaluated, providing a better understanding of the suitability of different simplifying assumptions for different ranges of power input.

To solve the highly nonlinear electro-thermal problem, a computational method is presented in which the domain of the thermal microactuator is discretized into finite elements. Using the Galerkin method, the weak forms of the governing heat balance equations are enforced throughout. Due to the nonlinearity of these governing equations, the weak forms are linearized and the nodal temperatures are iterated upon using Newton-Raphson iteration. A discussion of this computational method is presented in Section 3.2. The computational method and electro-thermal model are initially verified in Section 3.5.2 by comparing model predictions with the

experimentally measured temperatures for a V-shaped bent beam actuator presented in [52]. The model is then applied to the test actuator to provide additional experimental verification. Results and an investigation into the significance of nonlinearities in the model are compiled in Section 3.5.3.

3.2. Computational Method

Calculation of the actuator displacement first requires the evaluation of the electro-thermal response for use as the input to the thermo-mechanical model. In the computational method that follows, the governing differential equations, (20) and (21), will be converted into their weak form, and the actuator and air gap will be discretized into finite elements. Application of the Galerkin method with Newton-Raphson iteration will then permit the calculation of an approximate solution to (20) and (21). The resulting temperature field will be used as an input into (36). The reaction forces at the hot terminal will then be determined using (33), and the final steady state displacement of the actuator will be solved for using (40).

3.2.1.Mesh Strategy

Due to the large aspect ratio of each arm, the temperature can be assumed constant over the cross section. This permits the discretization of each arm into one-dimensional line elements to minimize computational cost. The temperature field in the air gap, however, can vary in the plane of the wafer (the x-y plane) but is assumed to remain uniform through the thickness of the actuator (the out-of-plane direction). The air gap is, therefore, discretized into two-dimensional quadrilateral elements. The mesh strategy is depicted in Fig. 8. To solve the nonlinear finite element problem, the two governing differential equations, (20) and (21), must be converted to weak form and enforced over the domain of each element.

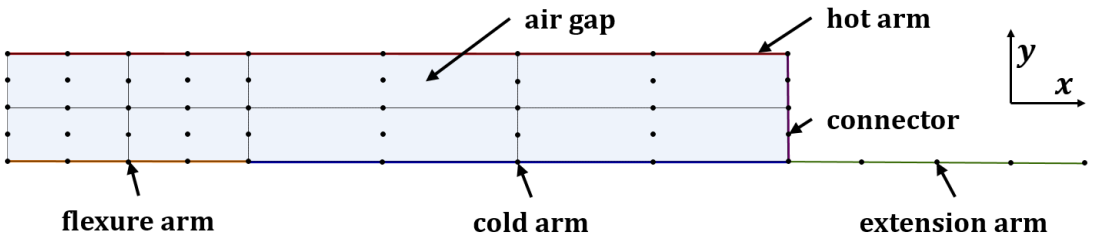

Fig. 8. Mesh strategy used for the discretization of the actuator and air gap.

3.2.2.Weak Formulation for the Heat Equation

For development of the weak form of the governing differential equations, (20) and (21) are first arranged in the form of a residual, $R(s)$ and $R(x,y)$ respectively, assuming steady state operating conditions. The temperature distribution that results in $R(s)=0$ and $R(x,y)=0$ over the entire domain is the solution to the differential equation. Equation (20) can first be rewritten as

$$R(s) = -k_{Si}(T)A\frac{d^2T(s)}{ds^2} - \frac{dk_{Si}(T)}{dT}A\left[\frac{dT(s)}{ds}\right]^2 + \varepsilon\sigma S_r[T(s)^4 - T_\infty^4] + h_{eq}(T)S_{cd}[T(s) - T_\infty] - J^2\rho(T)A = 0. \tag{41}$$

To derive the weak form, (41) is first multiplied by the weight function, $\psi(s)$ and integrated over the length of the domain, L.

$$R(s) = \int_0^L \left[-k_{Si}(T)A\frac{d^2T(s)}{ds^2} - \frac{dk_{Si}(T)}{dT}A\left[\frac{dT(s)}{ds}\right]^2 + \varepsilon\sigma S_r[T(s)^4 - T_\infty^4] + h_{eq}(T)S_{cd}[T(s) - T_\infty] - J^2\rho(T)A\right]\psi(s)\,ds = 0 \tag{42}$$

Applying integration by parts, (42) can be rewritten in the following weak form:

$$R(s) = -k_{Si}(T)A\frac{dT(s)}{ds}\psi(s)\Big|_0^L + \int_0^L \Big[k_{Si}(T)A\frac{dT(s)}{ds}\frac{d\psi(s)}{ds} + \varepsilon\sigma S_r[T(s)^4 - T_\infty^4]\psi(s) + h_{eq}(T)S_{cd}[T(s) - T_\infty]\psi(s) - J^2\rho(T)A\psi(s)\Big]\, ds = 0. \tag{43}$$

Similarly, the governing differential equation for the air gap, (21), can be arranged in residual form as follows:

$$R(x,y) = 2h_{eq}(T)[T(x,y) - T_\infty] - \boldsymbol{\nabla}\cdot[k_a(T)h\nabla T(x,y)] = 0 \tag{44}$$

This can also be written as:

$$R(x,y) = 2h_{eq}(T)[T(x,y) - T_\infty] - \frac{dk_a(T)}{dT}h\left[\left[\frac{\partial T(x,y)}{\partial x}\right]^2 + \left[\frac{\partial T(x,y)}{\partial y}\right]^2\right] - k_a(T)h\left[\frac{\partial^2 T(x,y)}{\partial x^2} + \frac{\partial^2 T(x,y)}{\partial y^2}\right] = 0. \tag{45}$$

Equation (45) can now be multiplied by the weight function, $\psi(x,y)$, and integrated over the domain, Ω, to obtain

$$R(x,y) = \iint_\Omega \left[2h_{eq}(T)[T(x,y) - T_\infty] - \frac{dk_a(T)}{dT}h\left[\left[\frac{\partial T(x,y)}{\partial x}\right]^2 + \left[\frac{\partial T(x,y)}{\partial y}\right]^2\right] - k_a(T)h\left[\frac{\partial^2 T(x,y)}{\partial x^2} + \frac{\partial^2 T(x,y)}{\partial y^2}\right]\right]\psi(x,y)\, dx\, dy = 0. \tag{46}$$

The order can now be reduced using partial integration, producing the following weak form:

$$R(x,y) = -\oint_{\partial\Omega} k_a(T)h\frac{dT(x,y)}{dn}\psi(x,y)ds + \iint_{\Omega}\left[2h_{eq}(T)[T(x,y)-T_{\infty}]\psi(x,y) + k_a(T)h\left[\frac{\partial T(x,y)}{\partial x}\frac{\partial\psi(x,y)}{\partial x}+\frac{\partial T(x,y)}{\partial y}\frac{\partial\psi(x,y)}{\partial y}\right]\right]dx\,dy = 0, \quad (47)$$

where n represents the normal to the boundary of the domain.

3.2.3.Galerkin Formulation

A solution to (43) and (47) is sought such that temperature in the one-dimensional actuator elements and two dimensional gap elements can be approximated by (48) and (49) respectively.

$$T(s) = \phi_j(s)c_j \quad (48)$$

$$T(x,y) = \phi_j(x,y)c_j \quad (49)$$

Here $c_j \in \mathbb{R}^n$ and represents a set of scalar coefficients to the shape functions, $\phi_j \in \mathbb{R}^n$. When applying the Galerkin method, the weight function is considered to be a linear combination of the shape functions. Therefore (43) can now be rewritten as:

$$F_i(c) = -k_{Si}\left(\phi_j(s)c_j\right)A\frac{d\left[\phi_j(s)c_j\right]}{ds}\phi_i(s)\Big|_0^L + \int_0^L\left[k_{Si}\left(\phi_j(s)c_j\right)A\frac{d\left[\phi_j(s)c_j\right]}{ds}\frac{d\phi_i(s)}{ds} + \varepsilon\sigma S_r\left[\left[\phi_j(s)c_j\right]^4 - T_{\infty}^4\right]\phi_i(s) + h_{eq}\left(\phi_j(s)c_j\right)S_{cd}\left[\left[\phi_j(s)c_j\right]-T_{\infty}\right]\phi_i(s) - J^2\rho\left(\phi_j(s)c_j\right)A\phi_i(s)\right]ds, \quad (50)$$

where F_i is the weak form of the residual after specifying the weight function and applying the approximations given by (48) and (49). This weak form of the residual is analogous to the load vector and will be referred to as such. Likewise, (47) can be rewritten as

$$\begin{aligned} F_i(c) = &- \oint_{\partial\Omega} k_a\big(\phi_j(x,y)c_j\big)h\frac{d\big[\phi_j(x,y)c_j\big]}{dn}\phi_i(x,y)\,dl \\ &+ \iint_{\Omega}\Bigg[k_a\big(\phi_j(x,y)c_j\big)h\Bigg[\frac{\partial\big[\phi_j(x,y)c_j\big]}{\partial x}\frac{\partial\phi_i(x,y)}{\partial x} \\ &+ \frac{\partial\big[\phi_j(x,y)c_j\big]}{\partial y}\frac{\partial\phi_i(x,y)}{\partial y}\Bigg] + 2h_{eq}\Big[\big[\phi_j(x,y)c_j\big] - T_\infty\Big]\phi_i(x,y)\Bigg]\,dx\,dy. \end{aligned} \tag{51}$$

3.2.4.Shape Functions

It is now necessary to define the set of shape functions to be used. In the presented method, each shape function is associated with a particular node such that ϕ_i corresponds with the i^{th} node. The shape functions are selected such that they evaluate to unity at their respective nodes and evaluate to zero at all other nodes. Moreover, the shape functions only evaluate to a nonzero value within the elements to which they are associated. This implies that, with regards to (48) and (49), the temperature at each node is equal to the value of the scalar coefficient, c_i, corresponding to that node. For the purposes of this work, it is sufficient to assume a set of quadratic Lagrangian shape functions such that each one-dimensional line element is composed of three nodes, and each two-dimensional quadrilateral element is composed of nine nodes. An overview of these shape functions is given in [53]. The element shape functions, ϕ_i^e, for the one-dimensional line elements are as follows:

$$\phi_1^e = \frac{1}{2}\xi(\xi - 1)$$

$$\phi_2^e = 1 - \xi^2 \tag{52}$$

$$\phi_3^e = \frac{1}{2}\xi(\xi + 1),$$

where ξ represents the local coordinate ranging from -1 to 1 on the master line element, shown in Fig. 9. The element shape functions for the two-dimensional quadrilateral elements are as follows:

$$\phi_1^e = \frac{1}{4}(\xi^2 - \xi)(\eta^2 - \eta)$$

$$\phi_2^e = \frac{1}{4}(\xi^2 + \xi)(\eta^2 - \eta)$$

$$\phi_3^e = \frac{1}{4}(\xi^2 + \xi)(\eta^2 + \eta)$$

$$\phi_4^e = \frac{1}{4}(\xi^2 - \xi)(\eta^2 + \eta) \tag{53}$$

$$\phi_5^e = \frac{1}{2}(1 - \xi^2)(\eta^2 - \eta)$$

$$\phi_6^e = \frac{1}{2}(\xi^2 + \xi)(1 - \eta^2)$$

$$\phi_7^e = \frac{1}{2}(1 - \xi^2)(\eta^2 + \eta)$$

$$\phi_8^e = \frac{1}{2}(\xi^2 - \xi)(1 - \eta^2)$$

$$\phi_9^e = (1 - \xi^2)(1 - \eta^2)$$

where ξ and η are local coordinates ranging from -1 to 1 and corresponding to the axes defined on the master quadrilateral element, also shown in Fig. 9. The subscript of each shape function described herein corresponds to the local node number to which the shape function is associated on the master element.

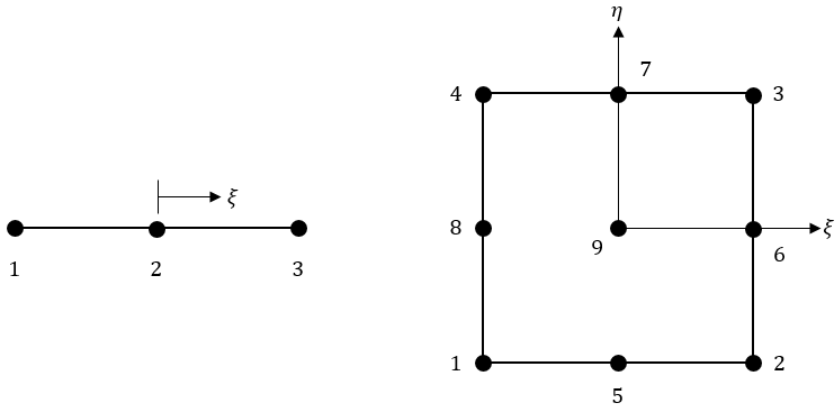

Fig. 9. Master element for a quadratic line element (left) and quadrilateral element (right).

To carry out the necessary computations for each element, that element is first transformed from the global coordinates to the local coordinates of the master element. For the geometry of this problem, the transformation for each line element is

$$\begin{aligned} s &= \frac{\xi}{2}[s_3 - s_1] + s_2 \\ ds &= \frac{1}{2}[s_3 - s_1]\, d\xi, \end{aligned} \tag{54}$$

where s_i is the s-coordinate associated with the i^{th} node on the master element. Similarly, the transformation for each quadrilateral element is

$$\begin{aligned} x &= \frac{\xi}{2}[x_6 - x_8] + x_9 \\ dx &= \frac{1}{2}[x_6 - x_8]\, d\xi \\ y &= \frac{\eta}{2}[y_7 - y_5] + y_9 \\ dy &= \frac{1}{2}[y_7 - y_5]\, d\eta, \end{aligned} \tag{55}$$

where x_i and y_i are the x- and y-coordinates respectively, associated with the i^{th} node on the master element. Equations (52), (53), (54), and (55) can now substituted into (50) and (51). The

integrals in (50) and (51) can then be performed with respect to the local coordinates on the master element (ranging from -1 to 1) to evaluate the elemental contribution to the global load vector. Equation (50) can now be rewritten to compute the element load vector F_i^e as follows:

$$\begin{aligned} F_i^e(c) = & -k_{Si}\big(\phi_j(\xi)c_j\big)A\frac{d\phi_j(\xi)}{d\xi}\frac{d\xi}{ds}c_j\phi_i(\xi)\Big|_{-1}^{1} \\ & + \int_{-1}^{1}\Bigg[k_{Si}\big(\phi_j(\xi)c_j\big)A\frac{d\phi_j(\xi)}{d\xi}\frac{d\xi}{ds}c_j\frac{d\phi_i(\xi)}{d\xi}\frac{d\xi}{ds} \\ & \quad + \varepsilon\sigma S_r\Big[\big[\phi_j(\xi)c_j\big]^4 - T_\infty^4\Big]\phi_i(\xi) \\ & \quad + h_{eq}\big(\phi_j(\xi)c_j\big)S_{cd}\Big[\big[\phi_j(\xi)c_j\big] - T_\infty\Big]\phi_i(\xi) \\ & \quad - J^2\rho\big(\phi_j(\xi)c_j\big)A\phi_i(\xi)\Bigg]\frac{ds}{d\xi}\,d\xi. \end{aligned} \tag{56}$$

Furthermore, (51) can be rewritten to compute the element load vector for the quadrilateral elements:

$$\begin{aligned} F_i^e(c) = & -\oint_{\partial\Omega^m} k_a\big(\phi_j(\xi,\eta)c_j\big)h\left[\frac{\partial\phi_j(\xi,\eta)}{\partial\xi}\frac{\partial\xi}{\partial n}c_j + \frac{\partial\phi_j(\xi,\eta)}{\partial\eta}\frac{\partial\eta}{\partial n}c_j\right]\phi_i(\xi,\eta)\,dl \\ & + \iint_{\Omega^m}\Bigg[k_a\big(\phi_j(\xi,\eta)c_j\big)h\Bigg[\frac{\partial\phi_j(\xi,\eta)}{\partial\xi}\frac{d\xi}{dx}c_j\frac{\partial\phi_i(\xi,\eta)}{\partial\xi}\frac{d\xi}{dx} \\ & \quad + \frac{\partial\phi_j(\xi,\eta)}{\partial\eta}\frac{d\eta}{dy}c_j\frac{\partial\phi_i(x,y)}{\partial\eta}\frac{d\eta}{dy}\Bigg] \\ & \quad + 2h_{eq}\Big[\big[\phi_j(\xi,\eta)c_j\big] - T_\infty\Big]\phi_i(\xi,\eta)\Bigg]\frac{dx}{d\xi}\frac{dy}{d\eta}\,d\xi\,d\eta, \end{aligned} \tag{57}$$

where Ω^m is the domain of the element in the coordinate system of the master element. As will be explained later, these integrals are carried out using 3 point Gaussian quadrature in the implementation of this computational method.

3.2.5.Newton-Raphson Method

The application of the Newton-Raphson iterative method first requires the linearization of the residual with respect to the unknown coefficients, c_j. A discussion of this can be found in [54]. The linearization of $F_i^e(c)$ for iteration k takes the following form:

$$K_{ij}^e\left(c^k\right) = \left.\frac{\partial F_i^e(c)}{\partial c_j}\right|_{c^k}, \tag{58}$$

where, $K_{ij}^e(c)$ is analogous to the elemental stiffness matrix. To compute the global stiffness matrix, the element stiffness matrix K_{ij}^e and element load vector F_i^e must be computed for each subdomain and compiled into global form by summing values at shared nodes [53]. The local nodal numbers are given the subscripts i and j in (58). These correspond to the nodal numbering of the master element and their respective shape functions [53]. The global stiffness matrix and load vector can now be assembled.

$$K_{mn} = \sum_e K_{pq}^e \tag{59}$$

$$F_m = \sum_e F_p^e \tag{60}$$

Here the subscripts p and q are used to denote the local nodal numbers on the master element corresponding with global node numbers m and n respectively. The summation in (59) and (60) is performed over all elements, and, if the element does not contain the nodes m and n, that element does not contribute to K_{mn}. An attempt can now be made to set the residual of the differential equation to zero.

$$F_m\left(c^{k+1}\right) \approx \left(c_n^{k+1} - c_n^k\right)K_{mn}\left(c^k\right) + F_m\left(c^k\right) = 0 \tag{61}$$

$$c_n^{k+1} = c_n^k - K_{mn}\left(c^k\right)^{-1} F_m\left(c^k\right) \tag{62}$$

3.2.6.Boundary Conditions

Before carrying out the iterative method described in Section 3.2.5, a temperature guess must first be applied to each node, allowing for an initial evaluation of K_{mn} and F_m. Each node is set to an initial temperature of T_∞, corresponding with the temperature in the unpowered state. A Dirichlet boundary condition is then enforced at all nodes located at the same x-position as the terminals. Because the terminals are considered to be large thermal masses, it is appropriate to fix the temperature at these nodes to that of the ambient environment, T_∞. To enforce this boundary condition, all members in the global stiffness matrix and global load vector corresponding with these nodes are removed. This ensures that $c_n^{k+1} = c_n^k = T_\infty$. A conduction boundary condition of the Neumann type is also enforced at the tip of the extension arm. This Neumann type boundary condition is captured by the first term in (50). When assembling the global load vector at nodes without applied Neumann type boundary conditions, the first terms in (50) and (51) sum to zero, enforcing the conservation of heat flux across the boundary of each element. This condition is given by

$$\begin{aligned} F_{m,0} = &\sum_{e_a} -k_{Si}\left(\phi_q(\xi)c_q\right) A \frac{d\phi_q(\xi)}{d\xi}\frac{d\xi}{ds} c_q \phi_p(\xi)\Big|_{-1}^{1} \\ &- \sum_{e_g} \oint_{\partial\Omega^m} k_a\left(\phi_q(\xi,\eta)c_q\right) h \left[\frac{\partial\phi_q(\xi,\eta)}{\partial\xi}\frac{\partial\xi}{\partial n} c_q \right. \\ &\left. + \frac{\partial\phi_q(\xi,\eta)}{\partial\eta}\frac{\partial\eta}{\partial n} c_q\right] \phi_p(\xi,\eta)\, dl = 0, \end{aligned} \tag{63}$$

where e_a is used to denote actuator elements and e_g is used to denote gap elements. This condition holds because all heat conducted out of an element, parallel to the x-y plane, is also conducted

into another element. The exception to this is along the actuator arms where heat is conducted to the external environment via the side of the actuator arm. However, because this external conduction boundary condition is captured in the integral of (50), including it in (63) would be redundant. Therefore, although the terms contained within (63) were included for completeness in the development of the computational method, they are not evaluated when calculating the element load vector or stiffness matrix unless a Neumann type boundary condition is to be applied (i.e. at the tip of the extension arm). This ensures conservation of heat flux in the x-y plane. To enforce the Neumann boundary condition at node p, corresponding with the local node number at the tip of the extension arm, the first term in (56), $F_{p,0}^{e}$, is evaluated as:

$$\begin{aligned} F_{p,0}^{e} &= -k_{Si}\big(\phi_j(\xi=1)c_j\big)A\frac{d\phi_j(\xi=1)}{d\xi}\frac{d\xi}{ds}c_j\phi_p(\xi=1) \\ &= h_{eq}\big(\phi_j(\xi=1)c_j\big)A_e\big[\phi_j(\xi=1)c_j - T_\infty\big] \\ &= h_{eq}\big(c_p\big)A_e\big[c_p - T_\infty\big]. \end{aligned} \tag{64}$$

In (64) A_e is the cross-sectional area at the tip of the extension arm. The contribution of $F_{p,0}^{e}$ to the element stiffness matrix, $K_{pq,0}^{e}$, must also be considered:

$$K_{pq,0}^{e} = \frac{d}{dc_q}\Big[h_{eq}\big(c_p\big)A_e\big[c_p - T_\infty\big]\Big]. \tag{65}$$

3.2.7.Error Analysis

To evaluate the error in the finite element approximation, the root sum of squares is calculated for the elements in the load vector. This is then normalized by the heat dissipated by the entire actuator. Iteration is performed until this value is less than an error parameter, χ. This criteria is given by

$$\frac{\sqrt{\sum F_i^2}}{I_{el}^2 R} < \chi. \tag{66}$$

3.3. Implementation of the Numerical Method

The presented computational method was implemented using the Python programming language. The "quad" function, which is a readily available general purpose numerical integration tool from the SciPy library, was used to carry out the integration for calculating the total resistance in the actuator, the thermal expansion in each arm, and the conduction shape factor. Furthermore, the integration required to compute the load vector and stiffness matrix was carried out using 3 point Gaussian quadrature.

3.4. Experimental Measurements

To verify the accuracy of the electro-thermal and thermo-mechanical models, it was necessary to compare model predictions with experimental measurements for the flexure actuator discussed in Section 2.1. Owing to the difficulty of experimentally measuring the temperature distribution in the microactuator, a combination of both current and displacement measurements were performed. A constant electrical potential difference ranging from 0 to 16.5 V was applied across the hot and cold arm terminals of the test actuator, and the current drawn by the actuator was measured using a Keithley 4200. The resulting displacement of the actuator was captured using an upright optical microscope. Captured images were then analyzed to extract the extension arm tip displacement corresponding with each applied voltage. The displacement of the actuator was measured with GetData digitizing software, using a 145 μm reference feature and a fixed origin. Both the voltage-displacement and current-voltage responses were used for model verification to help better ensure that the model predictions corresponded with the correct temperature magnitude and distribution in the device.

3.5. Results and Discussion

3.5.1.Mesh Convergence Study

A mesh convergence study was performed to determine the mesh fineness required to produce reliable results. In this study, both the fineness of the mesh and the significance of the error parameter, χ, were examined. Results of the study are shown in Fig. 10. Here, the parameter, n, is used to represent the number of elements with which the width of the gap and the lengths of the flexure arm, cold arm, and extension arm were meshed. For simplicity, each of these features was meshed with an equal number of elements. The hot arm was partitioned into two sections such that the first partition was directly opposite of the flexure arm and contained n elements, and the second partition was directly opposite of the cold arm and also contained n elements. This mesh strategy was illustrated in Fig. 8. The convergence of the model was quantified using the term, γ, defined by

$$\gamma = \sqrt{\sum_{i=1}^{16}\left(\frac{V - V_i^*}{V_i^*}\right)^2 + \sum_{i=1}^{16}\left(\frac{u_{tip} - u_{tip,i}^*}{u_{tip,i}^*}\right)^2}, \tag{67}$$

where V_i^* and $u_{tip,i}^*$ are reference values for the voltage drop across the actuator and the extension arm tip displacement respectively at a given electrical current input. In this study, the input into the model was an electrical current given by

$$I_{el} = (1.5 + 0.5i)\ \text{mA}, \tag{68}$$

where i ranged from 1 to 16. The reference values V_i^* and $u_{tip,i}^*$ were obtained from model results in which n =16 and χ =1×10^{-8} were assumed.

The results of the mesh convergence study indicate that, while the fineness of the mesh is significant in determining the upper limit of attainable convergence, the value selected for χ has

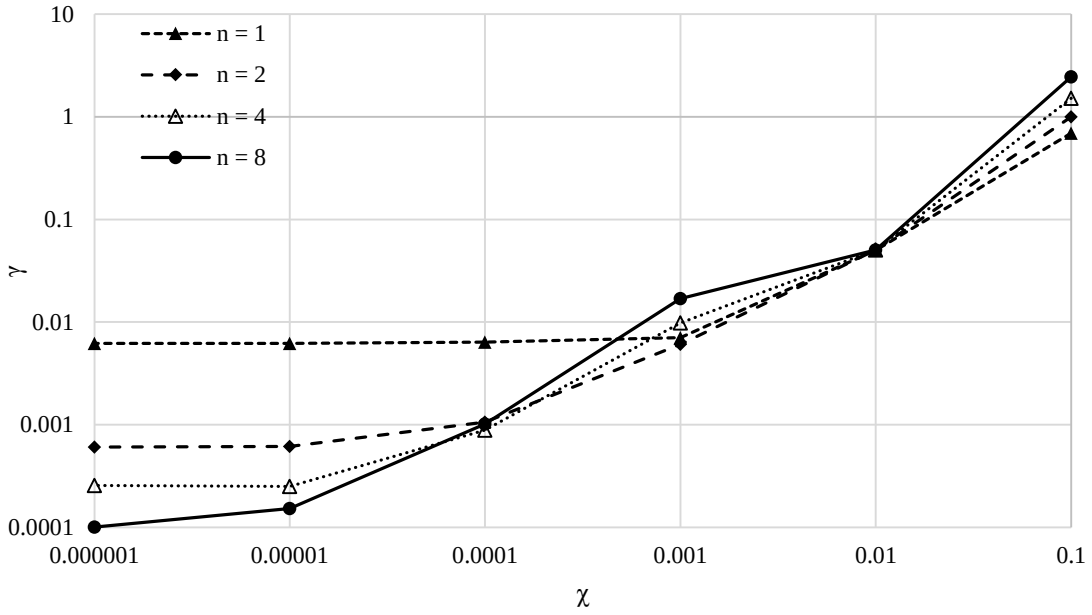

Fig. 10. Mesh convergence study.

far greater importance. Based on the findings of this study, values of $n = 2$ and $\chi = 1\times10^{-4}$ were selected for predicting the steady state performance of the flexure actuator. Selection of these values would permit both sufficient convergence and computational efficiency in the calculations that follow.

3.5.2.Literature-Based Verification of the Thermal Model and Computational Method

To verify the accuracy of the presented thermal model and computational method, they were first used to predict the temperature distribution in the P34 V-shaped bent-beam actuator presented in [52]. Geometry of the actuator corresponded with that presented in [52], and the temperature dependences of material properties were modeled using the relations reported in [38]. A mesh convergence study similar to that described in Section 3.5.1 was first performed to ensure the fidelity of the computations. A comparison of the model predictions with the experimental results (obtained using Raman thermometry in [52]) is shown in Fig. 11.

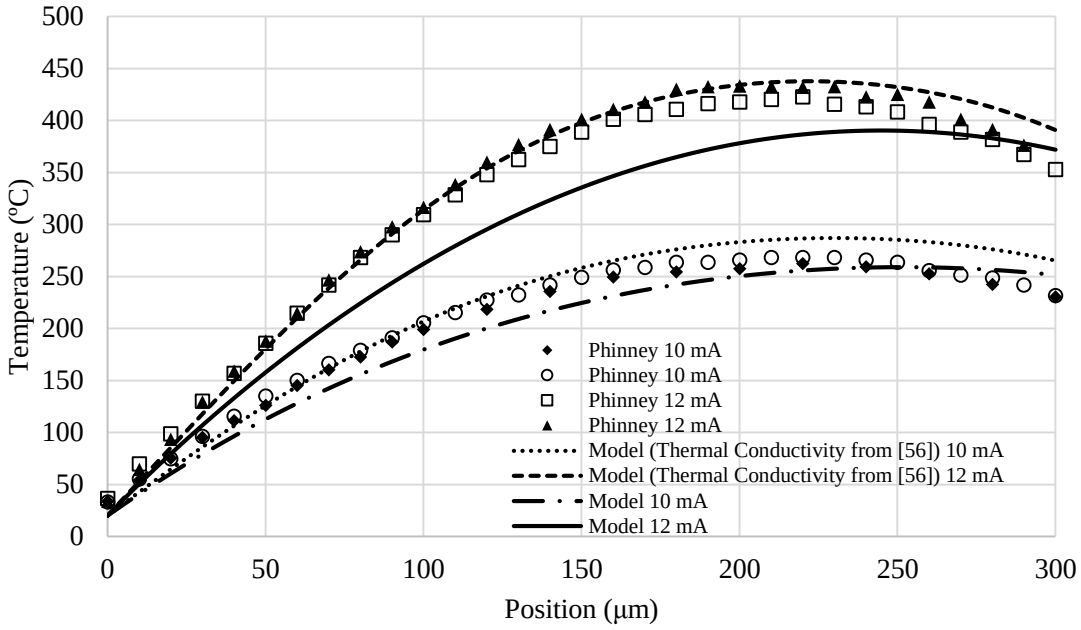

Fig. 11. Verification of the thermal model and computational method. Temperature measurements were performed in [52] with respect to position along one of the legs of the P34 V-shaped bent beam actuator.

Using the material properties outlined in [38], the model predictions were shown to deviate a significant amount from experimental results. However, a wide range of values have been reported in literature for the thermal conductivity of polysilicon due to variations in measurement techniques and fabrication processes [55]. Therefore, the temperature-dependent thermal conductivity measurements obtained from [56] for the fourth polysilicon layer of the SUMMiT V process (the same process used to fabricate the device in [52]) were curve fitted and incorporated into the model. Results using these thermal conductivity measurements are also included in Fig. 11 and show good agreement with the experimental measurements. Therefore, the results of this study are considered to provide sufficient confidence in the accuracy of the presented thermal model and computational approach.

3.5.3.Model Predictions and Experimental Verification

The thermal microactuator model was verified with experimental measurements obtained using the flexure actuator discussed previously. Furthermore radiation, intra-device heat transfer, and the temperature dependence of material properties were examined to determine their significance in producing accurate model predictions. The electrical current was selected as the input to the model, from which the steady state voltage drop across the actuator and extension arm tip displacement were calculated. To investigate the accuracy of the model, the relationship between current and voltage and the relationship between voltage and extension arm tip displacement were examined and compared with experimental data.

The thermal time constant, τ, was considered to be an unknown parameter in the model. Hence three different values were considered in the interest of investigating the significance of τ. Results are shown in Fig. 12, for which $\tau_1 = 0.5$ ms, $\tau_2 = 1.0$ ms, and $\tau_3 = 7.25$ ms. These thermal time constant values correspond with penetration depths of 105 μm, 149 μm, and 400 μm respectively. As will be shown in Section 4, τ_3 corresponds with the calculated value for the thermal time constant, obtained using the dynamic implementation of the model. However, as shown in Fig. 12, the predicted voltage-current and voltage-displacement responses show only slight τ dependence. Moreover, the model predictions match very well with experimental data. Both show a slight inflection point in the current-voltage response at an input current of ~7.2 mA, indicating that a portion of the actuator has approached the critical temperature at which resistivity begins to decrease. Because this inflection point occurs at approximately the same input current in both experimental measurements and model predictions (and because the voltage-current and displacement-voltage trends match very well), it can be deduced that the model accurately predicts the temperature of the device up until this point. It can be seen, however, that the current-voltage relationship begins to diverge at currents exceeding 7.2 mA. This discrepancy is likely the result

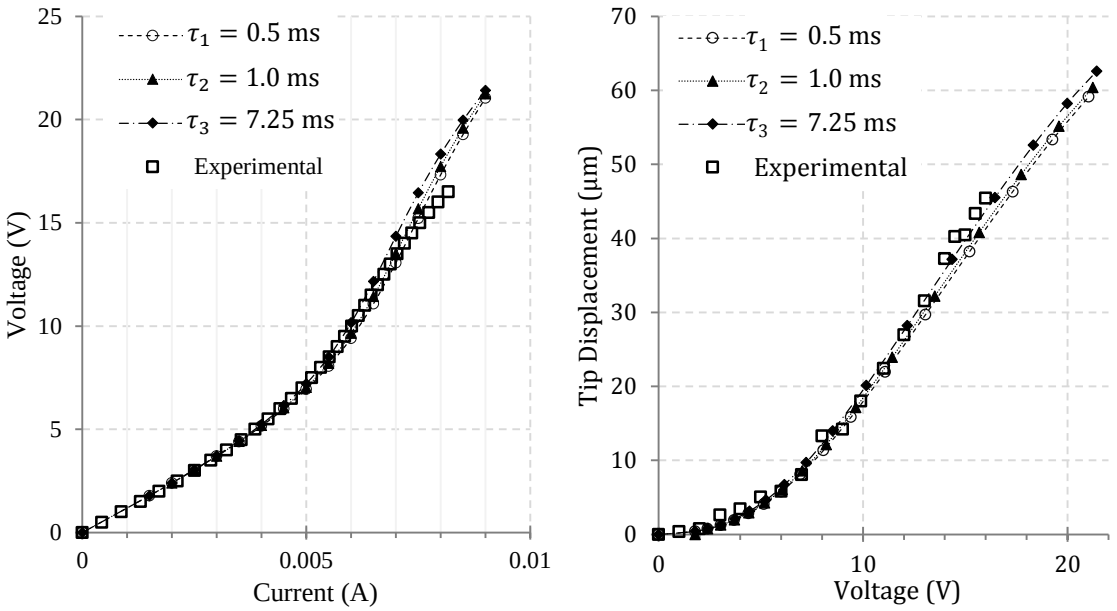

Fig. 12. Experimental verification of the thermal microactuator model, considering three different values for the thermal time constant. Displacement at the tip of the extension arm vs. applied voltage (left) and applied voltage vs. input current (right).

of a change in heat transfer path due to large displacements which is not taken into consideration in the model. As the actuator deforms, it approaches the side of the trench (see Fig. 1) and eventually passes over part of the substrate. With decreasing distance from the side of the trench, heat is removed more rapidly due to the close proximity to the substrate. This would decrease the resistance of the actuator, and, therefore, decrease the voltage drop across the device for a given current input. Because the model does not account for this change in conduction path, it slightly overestimates the voltage drop at high input powers.

The results presented in Fig. 12 are the predictions of what we consider the full model, which takes into account intra-device heat transfer, heat loss due to radiation, and the full temperature dependence of the thermal conductivity of silicon, thermal conductivity of air, electrical resistivity of silicon, and thermal expansion coefficient of silicon. The predictions of this model match experimental results very well. In addition to the full model already presented, six additional

hypothetical cases were modeled to illustrate the significance of each of the aforementioned sources of nonlinearity. Each of these models is identical to the full model, with the exception of a single modified parameter. Model 1 excludes the effects of intra-device heat transfer across the air gap, Model 2 excludes heat loss due to radiation, Model 3 assumes a temperature-independent value for the thermal conductivity of silicon (maintained at the room temperature value), Model 4 assumes a temperature-independent value for the thermal conductivity of air (maintained at the room temperature value), Model 5 assumes the temperature dependence of resistivity to be linearized about its room temperature value, and Model 6 assumes a temperature-independent value for the thermal expansion coefficient of silicon (maintained at the room temperature value).

A summary of these models is given in Table V. Because the thermal and mechanical problems have been decoupled, only the voltage-displacement relationship was examined for Model 6. As mentioned previously, the thermal time constant will be shown to be 7.25 ms using the dynamic implementation of the thermal microactuator model. Hence this value was used in all computations of these hypothetical models. A comparison of the model predictions is shown in Fig. 13, where the temperature field plot illustrated corresponds with an applied current input of 8 mA for all models.

TABLE V
OVERVIEW OF INVESTIGATED HYPOTHETICAL MODELS

Model 1	No intra-device heat transfer
Model 2	No heat loss due to radiation
Model 3	$k_{Si} = 146.6$ Wm^{-1}K^{-1} (Temperature-independent)
Model 4	$k_a = 0.026$ Wm^{-1}K^{-1} (Temperature-independent)
Model 5	$\rho_{Si} = 2.22 \times 10^{-5} + 3.93 \times 10^{-7} T$ Ω·m $\rho_c = -3.06 \times 10^{-7} + 5.38 \times 10^{-9} T$ Ω·m
Model 6	$\alpha = 2.57 \times 10^{-6}$ K^{-1} (Temperature-independent)

Overview of the models used to investigate the significance of different sources of nonlinearity. Each model is equivalent to the full model, with the exception of the modification listed in the adjacent column.

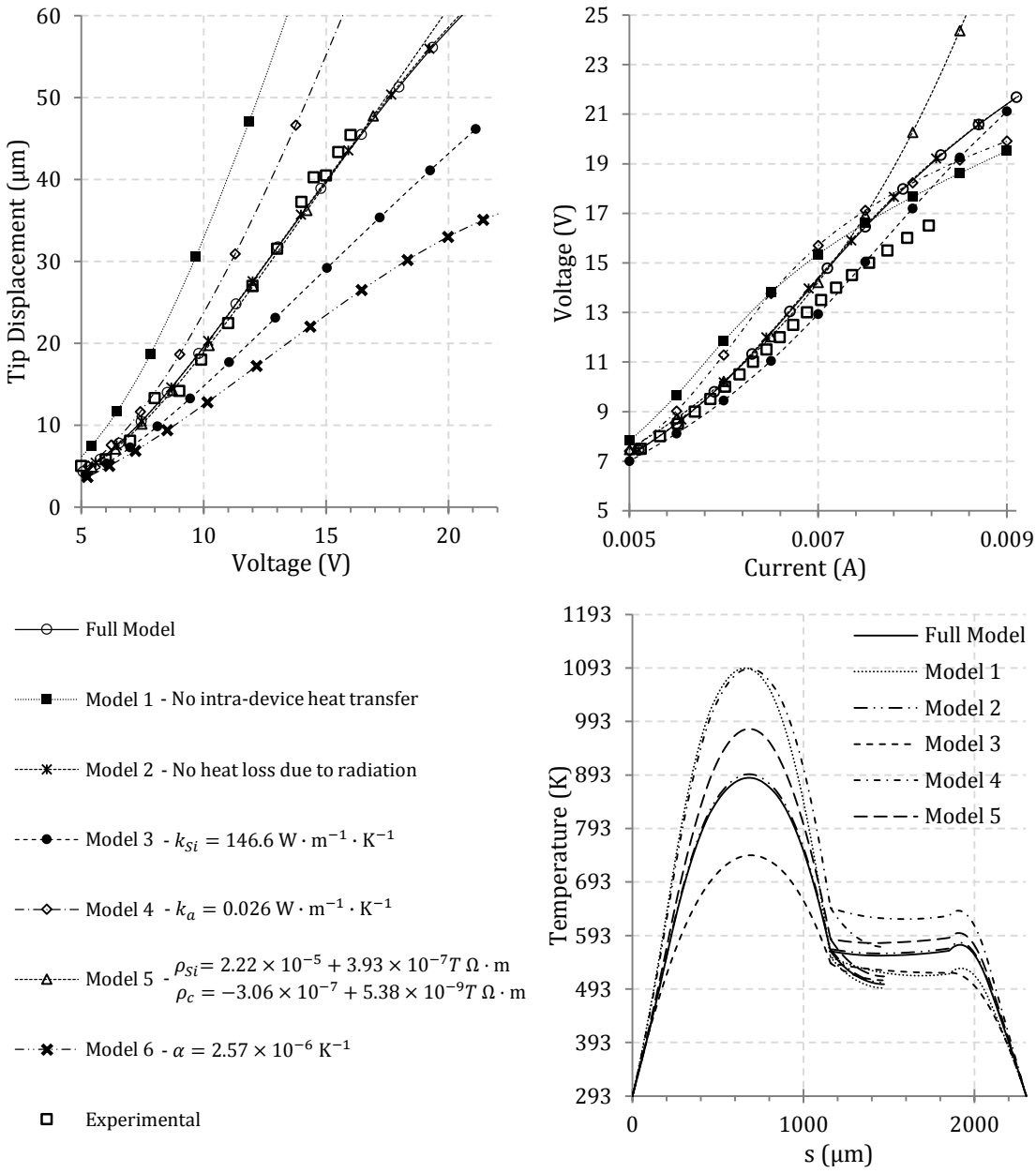

Fig. 13. Displacement at the tip of the extension arm vs. applied voltage (top left), applied voltage vs. input current (top right), and predicted temperature distribution given an input current of 8 mA (bottom right). All models are equivalent to the full model, except for the modifications shown in Table V.

In Model 4, the increase in the thermal conductivity of air with temperature was neglected, thus eliminating the temperature dependence of the heat transfer coefficient. Consequently, less heat was removed from the actuator through the air, and the predicted temperature was significantly higher than that predicted by the full model. This was especially significant in the hot arm, where the heat transfer coefficient should be expected to reach a maximum. The predicted displacement and voltage drop across the actuator in Model 4 were, therefore, noticeably larger than those predicted by the full model. At high input powers, however, the temperature was sufficiently high in the hot arm that resistivity began to decrease with increasing current, and the slope of the voltage-current response began to decrease. This is shown in the voltage-current plot of Fig. 13 by the pronounced inflection point, which occurs at a significantly lower input current than in experimental measurements, indicating an over-prediction of device temperature. As may be expected, a similar trend was observed in Model 1, which neglected intra-device heat transfer. In this case, however, the predicted temperature in the cold arm was lower than that predicted by the full model due to the absence of heat flux from the hot arm through the air gap. Furthermore, despite high operating temperatures, radiation was shown to have a minor effect on the temperature distribution in the actuator, as shown by the predictions of Model 2. Even at high input powers, the heat lost due to conduction was sufficiently large such that the effect of radiation was insignificant.

In Model 5, the assumption that electrical resistivity was linear in temperature yielded predictions similar to those of the full model at low to moderate input power. However, at high operating temperatures, the model overestimated electrical resistivity and, therefore, the heat generated via Joule heating. Model 5, therefore, over-predicted the temperature in the hot arm at high input power, resulting in over-prediction of displacement and voltage drop across the actuator. Model 3 neglected the decrease in the thermal conductivity of silicon that occurs with

increasing temperature, which resulted in significantly more heat conducted internally than in the full model. This prevented heat from accumulating as much in the hot arm, and, thus, Model 3 predicted a lower tip displacement and voltage drop than the full model. Though the voltage-current curve for Model 3 appears to match experimental measurements slightly better than the full model, the inflection point is not present, indicating an under-prediction of the device temperature. Model 6 was unable to capture the increase in the thermal expansion coefficient with temperature. Therefore, as expected, this model predicted a significantly lower tip displacement than the full model.

3.5.4.Effect of Elastic Modulus

Because there is insufficient data in the literature to characterize the temperature dependence of the elastic modulus of phosphorus-doped silicon, E was assumed to be temperature-independent in the implementation of the thermal microactuator model. To determine the validity of this assumption, an investigation was performed to examine the significance of considering the temperature dependence of the elastic modulus. For Boron doping in the range of 1.3×10^{15} to 8.5×10^{18} atoms/cm^3, the elastic modulus of <110> silicon can be modeled as:

$$E(T) = 1.51 \times 10^5(\text{eV})e^{\left(\frac{2.7\times10^{-3}(\text{eV})}{KT}\right)}(\text{MPa}) \tag{69}$$

from room temperature to 1273 K [41]. Here K is the Boltzmann constant. Though this relation is intended for Boron-doped silicon, (69) was used in this study to obtain an approximation of its effect on model predictions.

The consideration of the full temperature dependence of the elastic modulus required (34) to be numerically integrated over each arm of the actuator in the interest of computing the flexibility matrix. Calculating the displacement of the actuator also required the moment in (38) to be numerically integrated over the length of the hot arm. The displacement at the tip of the hot arm

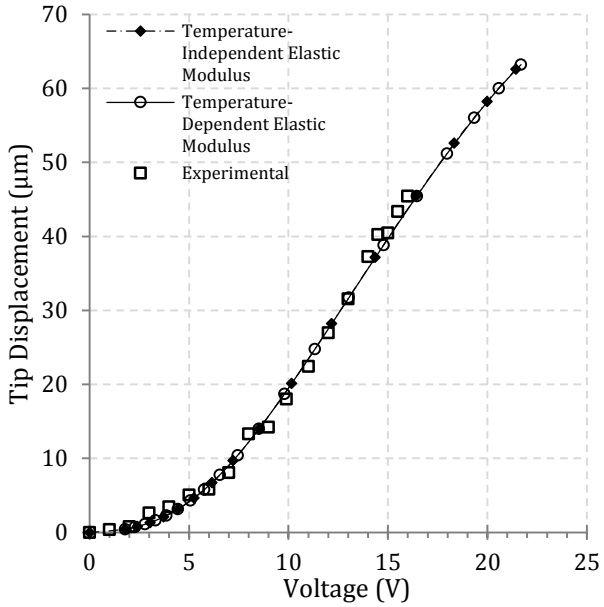

Fig. 14. Effect of neglecting the temperature dependence of the elastic modulus of silicon. Both plotted curves assume $\tau = 7.25$ ms, corresponding with $\delta_p = 400$ μm.

could then be extrapolated over the length of the extension arm to determine the extension arm tip displacement. Results from this study are shown in Fig. 14 and verify that assuming the elastic modulus of silicon to be temperature-independent has negligible effect on the accuracy of model predictions.

3.6. Conclusions

A computational method has been presented to permit the solution of the highly nonlinear governing heat equations for calculation of the steady state displacement of a thermal microactuator. The model employs the Galerkin method with Newton-Raphson iteration to fully account for radiation, intra-device heat transfer, and the full temperature dependence of material properties. The accuracy of the electro-thermal model and computational method presented herein were verified with experimental temperature measurements performed on a V-shaped bent beam actuator presented in [52]. The model was further verified using voltage, current, and extension

arm tip displacement measurements from experiments performed on a flexure actuator. For the first time, an analysis has been performed to determine the significance of each source of nonlinearity in the model, assuming a penetration depth of 400 μm which corresponds to a thermal time constant of 7.25 ms.

The results presented illustrate that, at relatively high current inputs, assuming the thermal conductivity of silicon to be temperature-independent underestimates the temperature in the device, causing the model to under-predict the extension arm tip displacement of the actuator. Similarly, assuming the thermal expansion coefficient of silicon to be temperature-independent also causes the model to significantly under-predict the displacement. Neglecting either intra-device heat transfer or the temperature dependence of the thermal conductivity of air, however, was shown to significantly over-predict the voltage drop and tip displacement for a given input current.

Radiation was shown to have a minor effect on the accuracy of the model, despite the high operating temperature of the hot arm. Thermal conduction is sufficiently large such that heat transferred due to radiation is negligible, even at high input powers. The findings of this study also indicate that assuming resistivity to be linear in temperature accurately predicts the performance of the actuator until high input powers, at which point the predictions begin to diverge from both experimental results and the full model predictions.

4. DYNAMIC MODELING

4.1. Introduction

It is very common in MEMS to use microactuators for high frequency applications, thus necessitating the prediction of the frequency response of thermal microactuators. To approximate the maximum frequency of operation for a given actuator, it is necessary to have appropriate models to predict the thermal behavior of the device over time.

In this regard, the dynamic performance of an out-of-plane thermal microactuator has been modeled in [37] using a finite difference method and the Runge-Kutta algorithm, and the dynamic performance of a flexure actuator has been modeled in [19] using a lumped model that incorporates both FEA and analytical methods. Transient models have also been developed in ANSYS to predict the behavior of flexure actuators [20, 33] and bent beam actuators [20]. A finite difference model was developed in [34] to predict the transient temperature rise in a bent beam actuator and in [36] to predict the temperature rise in a flexure actuator. Nodal analysis has also been used to investigate the dynamic behavior of flexure actuators in [29], and thermal networks have been used to predict temperature rise for general applications in thermal microactuators in [31].

Though these works have all presented methods for predicting transient behavior of thermal microactuators, it is desirable to permit the consideration of all nonlinearities introduced by radiation, intra-device heat transfer, and the nonlinear temperature dependence of material properties. This may allow for more accurate prediction of temperature distribution over time, and, therefore, permit the prediction of actuator displacement amplitude at different frequencies of operation.

To predict the dynamic behavior of thermal microactuators, the evolution of the temperature distribution in the actuator will first need to be computed. This requires the solution of the time-dependent electro-thermal model presented in Section 2.3.2. An initial temperature state will first

be assumed for the microactuator, and the temperature distribution at the end of a finite time step will be sought. The terms in (20) and (21) will be linearized with respect to time using the implicit Euler method and integrated over each time step. Equations (20) and (21) will then be converted to weak form, and the Galerkin method with Newton-Raphson iteration will be applied to predict the temperature distribution within the device at the end of each time step. The thermo-mechanical model presented in Section 2.3.3 will then be solved, permitting the calculation of the actuator displacement at the end of each time step.

In this chapter, the dynamic equation of motion will first be introduced in Section 4.2. A solution for the mechanical response of the actuator, however, will require knowledge of the transient thermal response, including the thermal time constant. In this regard, a computational method similar to that used in the previous chapter will be introduced in Section 4.3. This will then be applied to the test actuator in Section 4.5.2 to calculate the thermal time constant. After performing a modal analysis on the actuator, appropriate assumptions will be made to the dynamic equation of motion that will simplify the dynamic calculation of the tip displacement. Model predictions and experimental verification will then be discussed in Section 4.5.4.

4.2. Dynamic Equation of Motion

The motion of the actuator is governed by the following differential equation:

$$m\ddot{u} + d\dot{u} + k_m u = F_{th}(t), \tag{70}$$

where m is the effective mass of the actuator, d is the coefficient of damping, k_m is the mechanical stiffness, and F_{th} is the thermal force acting on the actuator due to thermal expansion in the arms. The natural frequency of most thermal microactuators, however, is sufficiently high that the dynamic response is limited by the rate at which temperature changes in the device. In cases where this is valid, (70) becomes

$$k_m u = F_{th}(t). \tag{71}$$

This implies that, provided the natural frequency is sufficiently large, the same thermo-mechanical model can be used to model the dynamic behavior as was used to model the steady state behavior. In this case, the transient effects are captured by the electro-thermal response.

Before any simplifying assumptions are made with regards to (70), it is necessary to model the transient thermal response of the actuator and estimate the thermal time constant. A modal analysis can then be performed to calculate the natural frequency of the primary mode of vibration, enabling a comparison to be made between the time scales of the mechanical response and the thermal response.

4.3. Computational Method

4.3.1. Weak Formulation

For development of the weak form of the governing differential equations to be used in dynamic computations, an implicit Euler method is first applied to the terms in (20) and (21). Contrary to the previous chapter, time dependence in (20) and (21) will be considered for this analysis. These equations will be integrated over each time step and arranged in the form of residuals, $R(s)$ and $R(x, y)$. For a given time step, the temperature distribution that results in $R(s) = 0$ and $R(x, y) = 0$ over the entire domain is the solution to the differential equation. Equation (20) will be considered first.

$$\begin{aligned} \varrho_{Si} c_{Si}(T) A \frac{\partial T(s,t)}{\partial t} = k_{Si}(T) A \frac{\partial^2 T(s,t)}{\partial s^2} + \frac{\partial k_{Si}(T)}{\partial T} A \left[\frac{\partial T(s,t)}{\partial s}\right]^2 + J(t)^2 \rho(T) A \\ - \varepsilon \sigma S_r [T(s,t)^4 - T_\infty^4] - h_{eq}(T) S_{cd} [T(s,t) - T_\infty] \end{aligned} \tag{72}$$

For a finite time step, Δt, this equation can be linearized and integrated using an implicit Euler strategy.

$$\int_{T_0}^{T} \varrho_{Si} c_{Si}(T) A \, \partial T(s,t) = \int_{t_0}^{t_0+\Delta t} \left[k_{Si}(T) A \frac{\partial^2 T(s,t)}{\partial s^2} + \frac{\partial k_{Si}(T)}{\partial T} A \left[\frac{\partial T(s,t)}{\partial s} \right]^2 \right.$$
$$+ J(t)^2 \rho(T) A - \varepsilon \sigma S_r [T(s,t)^4 - T_\infty^4] \tag{73}$$
$$\left. - h_{eq}(T) S_{cd} [T(s,t) - T_\infty] \right] \partial t$$

Within a single time step, each term on the right hand side will be considered a linear function of time, linearized about its value at the end of the time step. This is given by:

$$f = f_0 + \frac{df}{dt}\Big|_{t=\Delta t} t \tag{74}$$

where f represents the value of the term at time t measured from the beginning of the time step, and f_0 represents the value at the beginning of the time step. When integrated over the time step, one arrives at the following:

$$\int_{t=0}^{t=\Delta t} f \, dt = f_0 \Delta t + \frac{1}{2} \frac{df}{dt}\Big|_{t=\Delta t} \Delta t^2. \tag{75}$$

Now the term df/dt must be evaluated. To account for temperature dependence, this is evaluated using the chain rule:

$$\frac{df}{dt}\Big|_{t=\Delta t} = \frac{df}{dT}\Big|_{t=\Delta t} \frac{dT}{dt}\Big|_{t=\Delta t} = \frac{df}{dT}\Big|_{t=\Delta t} \frac{T - T_0}{\Delta t}. \tag{76}$$

Applying this to (73) and multiplying by the weight function produces

$$R(s,t) = -\int_0^L \left[\int_{T_0}^{T} \varrho_{Si} c_{Si}(T) A \, \partial T(s,t) \right] \psi(s) \, ds$$
$$+ C_{1m} + C_{2m} + C_{3m} + C_{4m} + C_{5m} = 0, \tag{77}$$

where

$$C_{1m} = \int_0^L \left[k_{Si}(T) A \frac{\partial^2 T(s,t)}{\partial s^2} \Delta t \Big|_{T=T_0} + \frac{1}{2} A \frac{\partial k_{Si}(T)}{\partial T} \frac{\partial^2 T(s,t)}{\partial s^2} [T(s,t) - T_0(s,t)] \Delta t \right.$$
$$\left. + \frac{1}{2} k_{Si}(T) A \left[\frac{\partial^2 T(s,t)}{\partial s^2} - \frac{\partial^2 T_0(s,t)}{\partial s^2} \right] \Delta t \right] \psi(s)\, ds \tag{78}$$

$$C_{2m} = \int_0^L \left[\frac{\partial k_{Si}(T)}{\partial T} A \left[\frac{\partial T(s,t)}{\partial s} \right]^2 \Delta t \Big|_{T=T_0} \right.$$
$$+ \frac{1}{2} \frac{\partial^2 k_{Si}(T)}{\partial T^2} A \left[\frac{\partial T(s,t)}{\partial s} \right]^2 [T(s,t) - T_0(s,t)] \Delta t \tag{79}$$
$$\left. + \frac{\partial k_{Si}(T)}{\partial T} A \frac{\partial T(s,t)}{\partial s} \left[\frac{\partial T(s,t)}{\partial s} - \frac{\partial T_0(s,t)}{\partial s} \right] \Delta t \right] \psi(s)\, ds$$

$$C_{3m} = \int_0^L \left[J_0(t)^2 \rho(T) A \Delta t|_{T=T_0} + \frac{1}{2} J(t)^2 \frac{\partial \rho(T)}{\partial T} A [T(s,t) - T_0(s,t)] \Delta t \right.$$
$$\left. + J(t) \rho(T) A [J(t) - J_0(t)] \Delta t \right] \psi(s)\, ds \tag{80}$$

$$C_{4m} = \int_0^L \left[-\varepsilon \sigma S_r [T(s,t)^4 - T_\infty^4] \Delta t|_{T=T_0} \right.$$
$$\left. - 2\varepsilon \sigma S_r T(s,t)^3 [T(s,t) - T_0(s,t)] \Delta t \right] \psi(s)\, ds \tag{81}$$

$$C_{5m} = \int_0^L \left[-h_{eq}(T) S_{cd} [T(s,t) - T_\infty] \Delta t \big|_{T=T_0} - \frac{1}{2} h_{eq}(T) S_{cd} [T(s,t) - T_0(s,t)] \Delta t \right.$$
$$\left. - \frac{1}{2} \frac{\partial h_{eq}(T)}{\partial T} S_{cd} [T(s,t) - T_\infty][T(s,t) - T_0(s,t)] \Delta t \right] \psi(s)\, ds. \tag{82}$$

The order of the differential equation must now be reduced using partial integration. The following are the applicable relations used for this equation:

$$\int_0^L k_{Si}(T)A\,\frac{\partial^2 T(s,t)}{\partial s^2}\psi(s)\Delta t\,ds = \left[k_{Si}(T)A\frac{\partial T(s,t)}{\partial s}\,\psi(s)\Delta t\right]\Bigg|_0^L$$
$$-\int_0^L \frac{\partial k_{Si}(T)}{\partial T}A\left[\frac{\partial T(s,t)}{\partial s}\right]^2\psi(s)\Delta t\,ds \tag{83}$$
$$-\int_0^L k_{Si}(T)A\frac{\partial T(s,t)}{\partial s}\frac{\partial \psi(s)}{\partial s}\Delta t\,ds$$

$$\int_0^L \frac{1}{2}\frac{\partial k_{Si}(T)}{\partial T}A\,\frac{\partial^2 T(s,t)}{\partial s^2}[T(s,t)-T_0(s,t)]\psi(s)\Delta t\,ds$$
$$=\left[\frac{1}{2}\frac{\partial k_{Si}(T)}{\partial T}A\frac{\partial T(s,t)}{\partial s}\,[T(s,t)-T_0(s,t)]\psi(s)\Delta t\right]\Bigg|_0^L$$
$$-\int_0^L \frac{1}{2}\frac{\partial^2 k_{Si}(T)}{\partial T^2}A\left[\frac{\partial T(s,t)}{\partial s}\right]^2[T(s,t)-T_0(s,t)]\psi(s)\Delta t\,ds \tag{84}$$
$$-\int_0^L \frac{1}{2}\frac{\partial k_{Si}(T)}{\partial T}A\frac{\partial T(s,t)}{\partial s}\left[\frac{\partial T(s,t)}{\partial s}-\frac{\partial T_0(s,t)}{\partial s}\right]\psi(s)\Delta t\,ds$$
$$-\int_0^L \frac{1}{2}\frac{\partial k_{Si}(T)}{\partial T}A\frac{\partial T(s,t)}{\partial s}[T(s,t)-T_0(s,t)]\frac{\partial \psi(s)}{\partial s}\Delta t\,ds$$

$$\int_0^L \frac{1}{2}k_{Si}(T)A\left[\frac{\partial^2 T(s,t)}{\partial s^2}-\frac{\partial^2 T_0(s,t)}{\partial s^2}\right]\psi(s)\Delta t\,ds$$
$$=\left[\frac{1}{2}k_{Si}(T)A\left[\frac{\partial T(s,t)}{\partial s}-\frac{\partial T_0(s,t)}{\partial s}\right]\psi(s)\Delta t\right]\Bigg|_0^L$$
$$-\int_0^L \frac{1}{2}\frac{\partial k_{Si}(T)}{\partial T}A\frac{\partial T(s,t)}{\partial s}\left[\frac{\partial T(s,t)}{\partial s}-\frac{\partial T_0(s,t)}{\partial s}\right]\psi(s)\Delta t\,ds \tag{85}$$
$$-\int_0^L \frac{1}{2}k_{Si}(T)A\left[\frac{\partial T(s,t)}{\partial s}-\frac{\partial T_0(s,t)}{\partial s}\right]\frac{\partial \psi(s)}{\partial s}\Delta t\,ds.$$

Equations (83)-(85) can now be inserted into the (78) and (79) to arrive at (86) which is, in turn, substituted back into (77) to arrive at the weak form of the differential equation.

$$
\begin{aligned}
C_{1m} + C_{2m} = \Bigg[& k_{Si}(T) A \frac{\partial T(s,t)}{\partial s} \psi(s) \Delta t \Big|_{T=T_0} \\
& + \frac{1}{2} k_{Si}(T) A \left[\frac{\partial T(s,t)}{\partial s} - \frac{\partial T_0(s,t)}{\partial s} \right] \psi(s) \Delta t \\
& + \frac{1}{2} \frac{\partial k_{Si}(T)}{\partial T} A \frac{\partial T(s,t)}{\partial s} [T(s,t) - T_0(s,t)] \psi(s) \Delta t \Bigg] \Bigg|_0^L \\
& + \int_0^L \Bigg[-k_{Si}(T) A \frac{\partial T(s,t)}{\partial s} \frac{\partial \psi(s)}{\partial s} \Delta t \Big|_{T=T_0} \\
& \quad - \frac{1}{2} \frac{\partial k_{Si}(T)}{\partial T} A \frac{\partial T(s,t)}{\partial s} [T(s,t) - T_0(s,t)] \frac{\partial \psi(s)}{\partial s} \Delta t \\
& \quad - \frac{1}{2} k_{Si}(T) A \left[\frac{\partial T(s,t)}{\partial s} - \frac{\partial T_0(s,t)}{\partial s} \right] \frac{\partial \psi(s)}{\partial s} \Delta t \Bigg] ds
\end{aligned}
\tag{86}
$$

Similarly, the governing differential equation for the air gap can be arranged in residual form as follows:

$$
\begin{aligned}
R(x,y,t) = & - \iint_\Omega \left[\int_{T_0}^{T} \varrho_a(T) c_a(T) h \, \partial T(x,y,t) \right] \psi(x,y) \, dx \, dy \\
& + C_{1g} + C_{2g} + C_{3g} = 0,
\end{aligned}
\tag{87}
$$

where

$$C_{1g} = \iint_{\Omega} \Big[k_a(T) h \boldsymbol{\nabla} \cdot \boldsymbol{\nabla} T(x,y,t)|_{T=T_0} \Delta t + \frac{1}{2} \frac{\partial k_a(T)}{\partial T} h \boldsymbol{\nabla} \cdot \boldsymbol{\nabla} T(x,y,t) \, [T(x,y,t) - T_0(x,y,t)] \Delta t + \frac{1}{2} k_a(T) h [\boldsymbol{\nabla} \cdot \boldsymbol{\nabla} T(x,y,t) - \boldsymbol{\nabla} \cdot \boldsymbol{\nabla} T_0(x,y,t)] \Delta t \Big] \psi(x,y) \, dx \, dy \tag{88}$$

$$C_{2g} = \iint_{\Omega} \Bigg[\frac{\partial k_a(T)}{\partial T} h \, [\boldsymbol{\nabla} T(x,y,t) \cdot \boldsymbol{\nabla} T(x,y,t)] \Delta t \Big|_{T=T_0} + \frac{1}{2} \frac{\partial^2 k_a(T)}{\partial T^2} h \, [\boldsymbol{\nabla} T(x,y,t) \cdot \boldsymbol{\nabla} T(x,y,t)][T(x,y,t) - T_0(x,y,t)] \Delta t + \frac{\partial k_a(T)}{\partial T} h \boldsymbol{\nabla} T(x,y,t) \cdot [\boldsymbol{\nabla} T(x,y,t) - \boldsymbol{\nabla} T_0(x,y,t)] \Delta t \Bigg] \psi(x,y) \, dx \, dy \tag{89}$$

$$C_{3g} = -\iint_{\Omega} \Big[h_{eq}(T) S_{cd} [T(x,y,t) - T_\infty] \Delta t \Big|_{T=T_0} + \frac{1}{2} h_{eq}(T) S_{cd} [T(x,y,t) - T_0(x,y,t)] \Delta t + \frac{1}{2} \frac{\partial h_{eq}(T)}{\partial T} S_{cd} [T(x,y,t) - T_\infty][T(x,y,t) - T_0(x,y,t)] \Delta t \Big] \psi(x,y) \, dx \, dy. \tag{90}$$

Now integration by parts must be employed to reduce the order of the equation. The applicable relations are the following:

$$\iint_{\Omega} k_a(T) h\boldsymbol{\nabla}\cdot\boldsymbol{\nabla}T(x,y,t)\,\psi(x,y)\Delta t\,dx\,dy$$

$$= \oint_{\partial\Omega} k_a(T) h\boldsymbol{\nabla}T(x,y,t)\psi(x,y)\Delta t\,dl$$

$$- \iint_{\Omega} \frac{\partial k_a(T)}{\partial T} h\boldsymbol{\nabla}T(x,y,t)\cdot\boldsymbol{\nabla}T(x,y,t)\psi(x,y)\Delta t\,dx\,dy \tag{91}$$

$$- \iint_{\Omega} k_a(T) h\boldsymbol{\nabla}T(x,y,t)\cdot\boldsymbol{\nabla}\psi(x,y)\Delta t\,dx\,dy$$

$$\iint_{\Omega} \frac{1}{2}\frac{\partial k_a(T)}{\partial T} h\boldsymbol{\nabla}\cdot\boldsymbol{\nabla}T(x,y,t)[T(x,y,t)-T_0(x,y,t)]\,\psi(x,y)\Delta t\,dx\,dy$$

$$= \oint_{\partial\Omega} \frac{1}{2}\frac{\partial k_a(T)}{\partial T} h\boldsymbol{\nabla}T(x,y,t)[T(x,y,t)-T_0(x,y,t)]\psi(x,y)\Delta t\,dl$$

$$- \iint_{\Omega} \frac{1}{2}\frac{\partial^2 k_a(T)}{\partial T^2} h\boldsymbol{\nabla}T(x,y,t)$$

$$\cdot\boldsymbol{\nabla}T(x,y,t)[T(x,y,t)-T_0(x,y,t)]\psi(x,y)\Delta t\,dx\,dy \tag{92}$$

$$- \iint_{\Omega} \frac{1}{2}\frac{\partial k_a(T)}{\partial T} h\boldsymbol{\nabla}T(x,y,t)$$

$$\cdot[\boldsymbol{\nabla}T(x,y,t)-\boldsymbol{\nabla}T_0(x,y,t)]\psi(x,y)\Delta t\,dx\,dy$$

$$- \iint_{\Omega} \frac{1}{2}\frac{\partial k_a(T)}{\partial T} h\boldsymbol{\nabla}T(x,y,t)$$

$$\cdot\boldsymbol{\nabla}\psi(x,y)[T(x,y,t)-T_0(x,y,t)]\Delta t\,dx\,dy$$

$$\iint_{\Omega} \frac{1}{2} k_a(T) h[\boldsymbol{\nabla} \cdot \boldsymbol{\nabla} T(x,y,t) - \boldsymbol{\nabla} \cdot \boldsymbol{\nabla} T_0(x,y,t)] \psi(x,y) \Delta t \, dx \, dy$$

$$= \oint_{\partial\Omega} \frac{1}{2} k_a(T) h[\boldsymbol{\nabla} T(x,y,t) - \boldsymbol{\nabla} T_0(x,y,t)] \psi(x,y) \Delta t \, dl$$

$$- \iint_{\Omega} \frac{1}{2} \frac{\partial k_a(T)}{\partial T} h[\boldsymbol{\nabla} T(x,y,t) - \boldsymbol{\nabla} T_0(x,y,t)] \cdot \boldsymbol{\nabla} T(x,y,t) \psi(x,y) \Delta t \, dx \, dy \tag{93}$$

$$- \iint_{\Omega} \frac{1}{2} k_a(T) h[\boldsymbol{\nabla} T(x,y,t) - \boldsymbol{\nabla} T_0(x,y,t)] \cdot \boldsymbol{\nabla} \psi(x,y) \Delta t \, dx \, dy.$$

Now these relations can be substituted back into (88) and (89) to arrive at (94). This is, in turn, substituted back into (87) to produce the weak form of the differential equation for the air gap.

$$\begin{aligned} C_{1g} + C_{2g} = \oint_{\partial\Omega} \Bigg[& k_a(T) h \boldsymbol{\nabla} T(x,y,t)|_{T=T_0} \\ & + \frac{1}{2} \frac{\partial k_a(T)}{\partial T} h \boldsymbol{\nabla} T(x,y,t)[T(x,y,t) - T_0(x,y,t)] \\ & + \frac{1}{2} k_a(T) h[\boldsymbol{\nabla} T(x,y,t) - \boldsymbol{\nabla} T_0(x,y,t)] \Bigg] \psi(x,y) \Delta t \, dl \\ - \iint_{\Omega} \Bigg[& k_a(T) h \boldsymbol{\nabla} T(x,y,t) \cdot \boldsymbol{\nabla} \psi(x,y)|_{T=T_0} - \frac{1}{2} \frac{\partial k_a(T)}{\partial T} h \boldsymbol{\nabla} T(x,y,t) \\ & \cdot \boldsymbol{\nabla} \psi(x,y)[T(x,y,t) - T_0(x,y,t)] \\ & - \frac{1}{2} k_a(T) h[\boldsymbol{\nabla} T(x,y,t) - \boldsymbol{\nabla} T_0(x,y,t)] \cdot \boldsymbol{\nabla} \psi(x,y) \Bigg] \Delta t \; dx \, dy \end{aligned} \tag{94}$$

4.3.2.Iterative Approach

To solve for the time evolution of the temperature distribution in the actuator, the same solution approach can be applied as in Sections 3.2.3 through 3.2.7. In this case, the temperature distribution at the end of the previous time step is specified as the initial condition. The Galerkin

method is then applied at each time step, replacing the weight function with shape functions and iteratively solving for the temperature distribution using Newton-Raphson iteration. Because MEMS actuators are most often controlled by inputting a potential function, the applied voltage has been selected as the input to the dynamic problem. During the first iteration of each time step, the electrical current input to the actuator is calculated based on the temperature distribution at the end of the previous time step. This means that during the first Newton-Raphson iteration for each time step, $J = J_0$. In each of the following iterations, the electrical current is updated using (29), based on the most recently calculated temperature distribution. As shown in the previous section, both J and J_0 are required to evaluate each element of the load vector. Therefore, to evaluate whether χ is sufficiently small to warrant proceeding to the next time step, the load vector must be reevaluated with the updated value of J following each Newton-Raphson iteration.

4.4. Experimental Methods

Due to the difficulty of directly measuring device displacement at high frequency, verification of the dynamic implementation of the model was performed by applying a potential difference across the hot and cold terminals and measuring the current drawn by the device over time. The purpose of this experiment was to verify the time response predicted by the model.

A voltage was applied to the actuator with an Agilent 33220A signal generator. A 1.01 Ω shunt resistor was placed in series with the device, and the potential drop across the resistor was measured to calculate the current flow through the circuit. The voltage drop was also measured across the actuator itself and used as the input to the microactuator model for model verification. Measurements were taken in LabView using a National Instruments USB-6211 at a sample rate of 20 kHz. The highest potential drop across the actuator that could be achieved using the signal generator was 9.6 V, and, therefore, this value was used for many of the dynamic computations.

4.5. Results and Discussion

4.5.1. Convergence Study

A convergence study was performed to determine an acceptable range for the size of each time step, Δt, and the magnitude of the error parameter, χ, used in the computational method. Because a mesh convergence study was already performed in Section 3.5.1, a mesh corresponding with $n = 2$ was assumed for all calculations in this study and all other computations involving the dynamic implementation of the thermal microactuator model henceforth. In this study, several different time steps were considered: 1 ms, 0.5 ms, 0.25 ms, and 0.125 ms. A voltage input of 9.6 V was applied as the electrical input to the problem, and the current draw and extension arm tip displacement were calculated from time $t = 0$ to $t = 30$ ms. Similar to how the mesh convergence study was performed in Section 3.5.1, all predictions were compared with those corresponding to a reference time step and error parameter value. For this study 0.1 ms was selected for the reference value of Δt, and 1×10^{-14} was selected for the reference value of χ. The following equation was then used to quantify convergence:

$$\lambda = \sqrt{\sum_{i=1}^{30}\left(\frac{I - I_i^*}{I_i^*}\right)^2 + \sum_{i=1}^{30}\left(\frac{u_{tip} - u_{tip,i}^*}{u_{tip,i}^*}\right)^2}, \tag{95}$$

where I^* is the calculated current draw of the reference at a given time, and u_{tip}^* is the calculated extension arm tip displacement of the reference at a given time. To ensure compatibility of results regardless of time step size, the calculation of λ included predictions at 30 different times, t, where $t = i$ ms. Results of this study are presented in Fig. 15. From the findings, a maximum allowable step size of $\Delta t = 0.5$ ms and a value of $\chi = 10^{-8}$ were selected to be used for the remainder of the computations involving the dynamic implementation of the model.

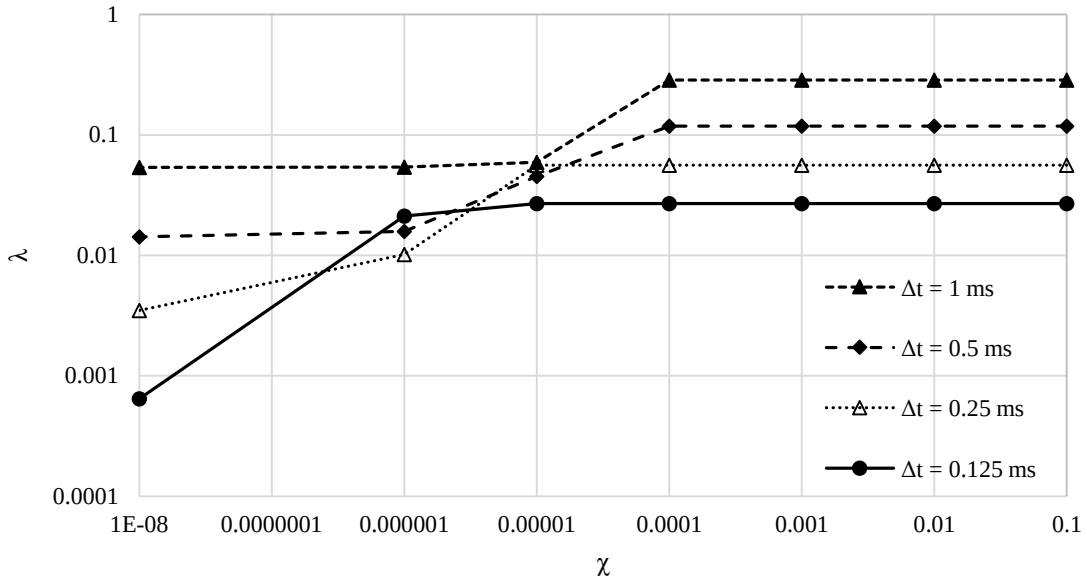

Fig. 15. Convergence study performed to determine an acceptable range for the size of each time step, Δt, and the magnitude of the error parameter, χ, used in the computational method.

4.5.2.Computation of the Thermal Time Constant

The value of the thermal time constant can be approximated by considering the actuator response to a pulse-width modulated voltage input with 50% duty cycle. When voltage is applied, the temperature, and therefore the resistance, of the actuator rises. The reverse occurs when voltage is removed, causing the resistance to oscillate between a maximum peak value and a minimum peak value. At very low frequencies, the actuator has ample time to reach thermal equilibrium, and the peak to peak resistance is at a maximum. As the frequency of the electrical input is increased, a frequency is eventually reached at which the actuator no longer has sufficient time to reach a thermal equilibrium, causing the peak to peak resistance to decrease. To approximate the thermal time constant, the frequency of the electrical input required to reduce the peak to peak resistance to 70% (-3 dB) the maximum peak to peak resistance is considered [57]. This frequency is denoted by f_{3dB}. The thermal time constant is then given by

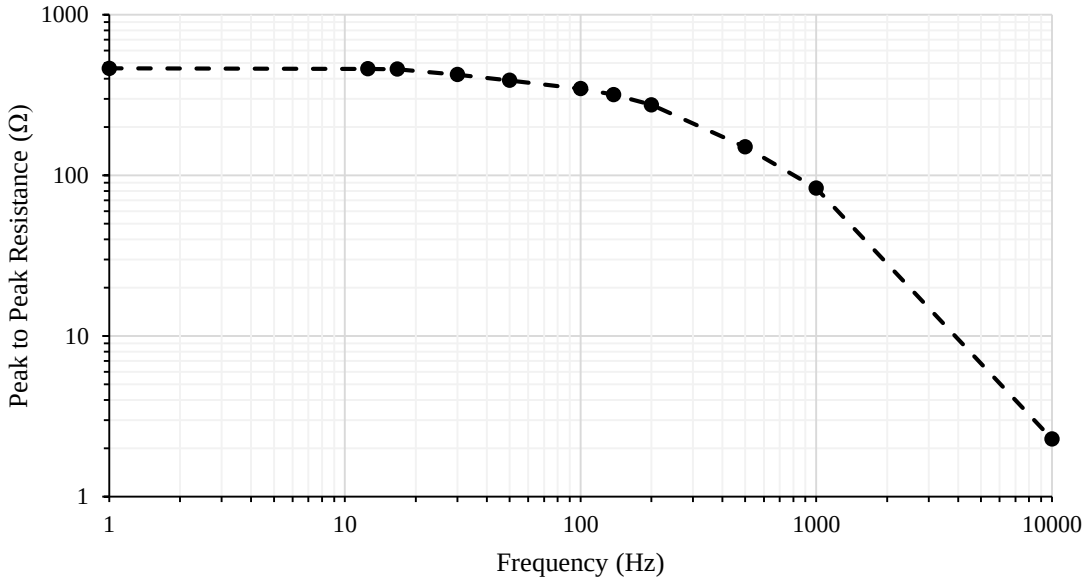

Fig. 16. Peak to peak resistance at different frequencies of applied voltage using a pulse-width modulated signal at 50% duty cycle and 9.6 Vpp.

$$\tau = \frac{1}{f_{3dB}}. \tag{96}$$

To determine the thermal time constant of the flexure actuator, a pulse-width modulated voltage with 50% duty cycle and 9.6 Vpp was applied as the input to the dynamic model. The resulting temperature distribution was calculated over time using at least 20 time steps per period, ensuring that the maximum time step was no larger than 0.5 ms to achieve appropriate convergence. At each frequency observed, the peak to peak resistance was calculated [see (28) for the calculation of the total actuator resistance] after a steady state waveform was achieved. The results of this analysis are shown in Fig. 16. From these findings, it was found that f_{3dB}, corresponding with a peak to peak resistance of 70% the maximum peak to peak resistance, was

achieved at a frequency of approximately 138 Hz. Hence the thermal time constant is approximately 7.25 ms. This, in turn, corresponds with a thermal penetration depth of 400 μm, which will be used for the remaining computations.

4.5.3.Natural Frequency

A modal analysis was performed in ABAQUS to determine the natural frequency of the primary mode of vibration. If the natural frequency is sufficiently high the thermo-mechanical problem can be modeled quasi-statically. The test actuator was modeled in ABAQUS and meshed with 20 node three dimensional brick elements. Both the terminal face of the hot arm and flexure arm were constrained against displacement and rotation in all directions. As shown in Fig. 17, the primary mode of vibration was found to be 8.7 kHz. Because the thermal time constant was found to be 7.25 ms, the actuator can be considered to reach mechanical equilibrium much faster than it reaches thermal equilibrium. Thus the same thermo-mechanical model that was used for the steady state problem can also be used for predicting the dynamic response.

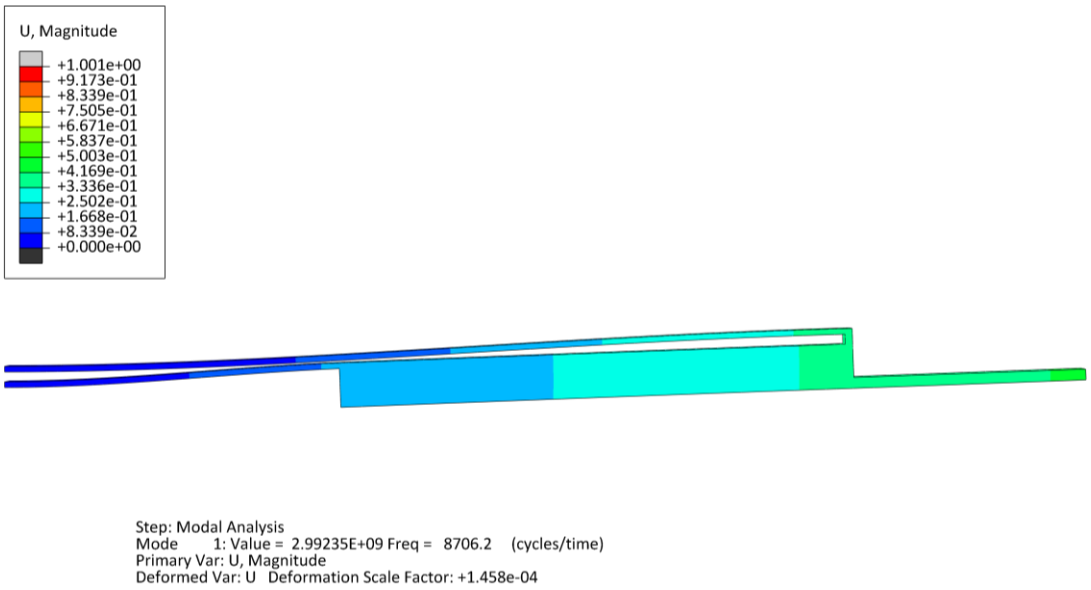

Fig. 17. Modal analysis in ABAQUS.

4.5.4.Dynamic Model Predictions and Experimental Verification

To verify the accuracy of the dynamic model three different DC voltages were applied to the test actuator using a signal generator. The resulting current flow was measured over time and the resistance in the actuator was calculated. These were then compared with the predictions of the dynamic implementation of the thermal microactuator model. Results illustrating the current-time response of the actuator and the model predictions are shown in Fig. 18. The trends illustrated for the experimental measurements and model predictions are slightly offset due to the imperfect current-voltage predictions of the model, but the significance of these results is in the time response. Though the model predicts a slightly faster time response, it appears to show good agreement with experimental results.

To further illustrate the transient behavior and to examine the significance of the nonlinearities previously discussed (see Table V), the ratio of the rise in resistance to the total rise in resistance at steady state is shown in Fig. 19 for a 9.6 V input. This ratio is given by

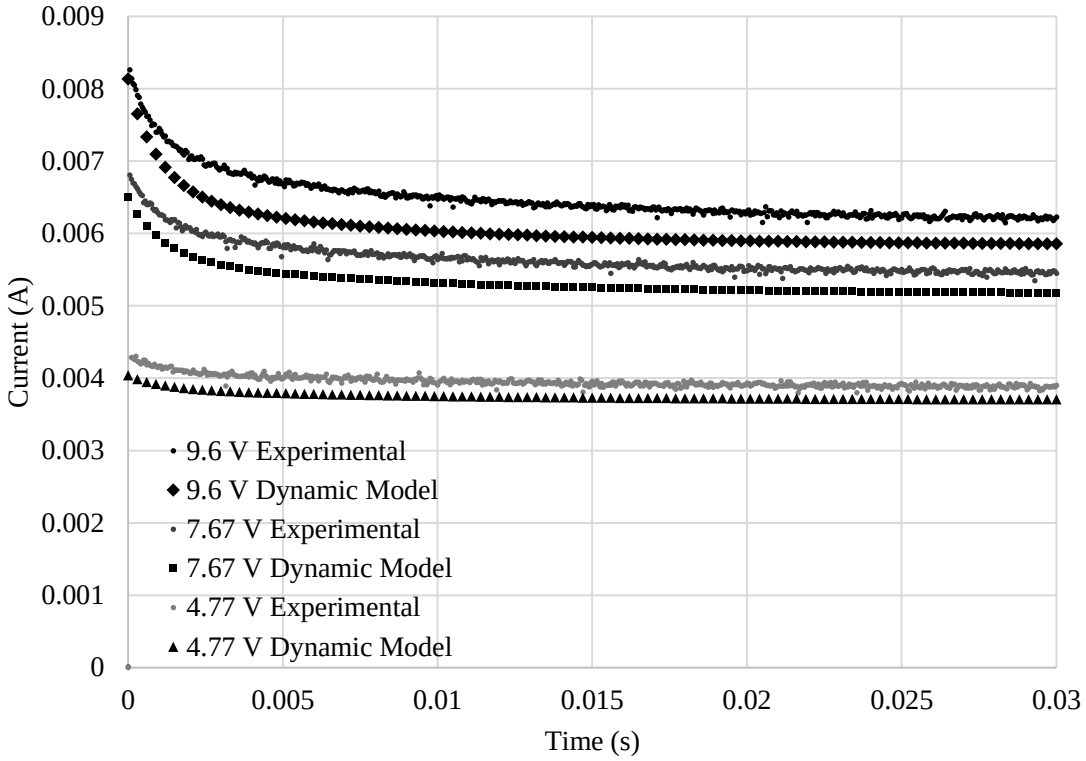

Fig. 18. Transient current response of the test actuator and corresponding model predictions.

$$\mu = \frac{[R(t) - R(t=0)]}{[R(t=\infty) - R(t=0)]}. \tag{97}$$

As shown in Fig. 19, the model predicts a faster initial rise time than that found experimentally. However, the time required to reach $\mu \approx 1$ is comparable. It is also shown that the assumptions made in Models 1, 3, and 4 do not significantly affect the predicted time response of the actuator (Models 2 and 5 were not considered because in Section 3.5.3 they were shown to be insignificant at 9.6 V). However, the time response of Model 4 presents a slight improvement over the full model and can offer some insight into the shortcomings of the presented full model. Model 4, which assumes a temperature-independent value for the thermal conductivity of air, applies a temperature-independent (and, therefore, time-independent) heat transfer coefficient. This is

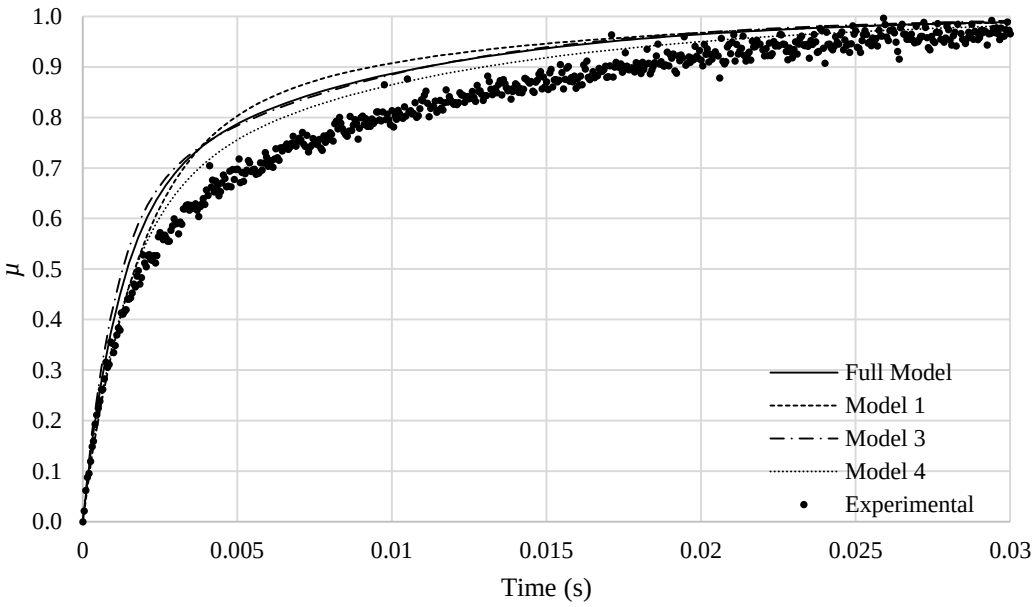

Fig. 19. Ratio of the rise in resistance to the total rise in resistance at steady state with respect to time, assuming 9.6 V input.

contrary to the full model, which applies a heat transfer coefficient that increases with temperature, and, therefore, increases over time. A likely reason for the discrepancy between the model and experimental results is that the temperature gradients in the air surrounding the actuator change over time. Initially, after the actuator has been heated slightly but heat has not yet had enough time to diffuse radially, there exists a large temperature gradient in the air surrounding the actuator (i.e. a small penetration depth). This creates a higher heat transfer coefficient than is predicted by the thermal microactuator model. As time advances, heat begins to diffuse radially outward from the actuator, reducing this temperature gradient (eventually reaching the gradient predicted by the full model at $t = \tau$). This has the effect of reducing $h_{eq}(T)$ over time. Hence, the time dependence of the penetration depth increases the time required for the temperature to rise. Because the presented model assumes the penetration depth to be constant, it predicts a slightly faster time response.

Fig. 20 and Fig. 21 illustrate the effect of signal frequency on the total resistance of the actuator and the displacement at the tip of the extension arm, respectively, assuming a 9.6 Vpp pulse-width modulated input with 50% duty cycle. As is shown, at frequencies significantly higher than f_{3dB}, the time response of both the resistance and the tip displacement approaches a form that largely resembles the response for a DC voltage input, scaled down in magnitude. As may be expected, this is because, when the applied voltage is set to zero, the actuator is not allowed sufficient time to cool before the voltage is again applied. As frequency is increased, the device is permitted less time to cool, causing the waveform to converge toward the response of a reduced DC voltage input. As time progresses, the resistance and tip displacement eventually reach steady state values around which they oscillate slightly. Furthermore, as can be seen in Fig. 21 at low frequency, the extension arm reaches a maximum displacement before decreasing to a steady state value. Likewise, during cooling, the displacement actually becomes negative before approaching zero. This is due to the larger thermal mass of the cold arm relative to the hot arm. As the device heats up, the hot arm reaches steady state before the cold arm. As the temperature in the cold arm increases to its steady state temperature, the thermal expansion mismatch between the hot arm and the cold arm and, therefore the displacement, is reduced. The reverse is true during cooling.

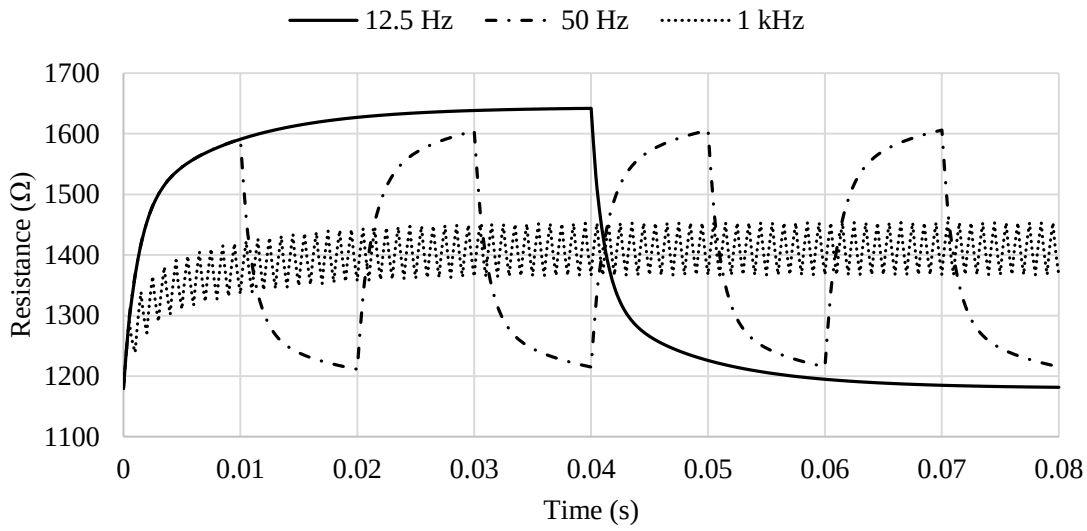

Fig. 20. Frequency response of the total actuator resistance, assuming a 9.6 Vpp pulse-width modulated input with 50% duty cycle.

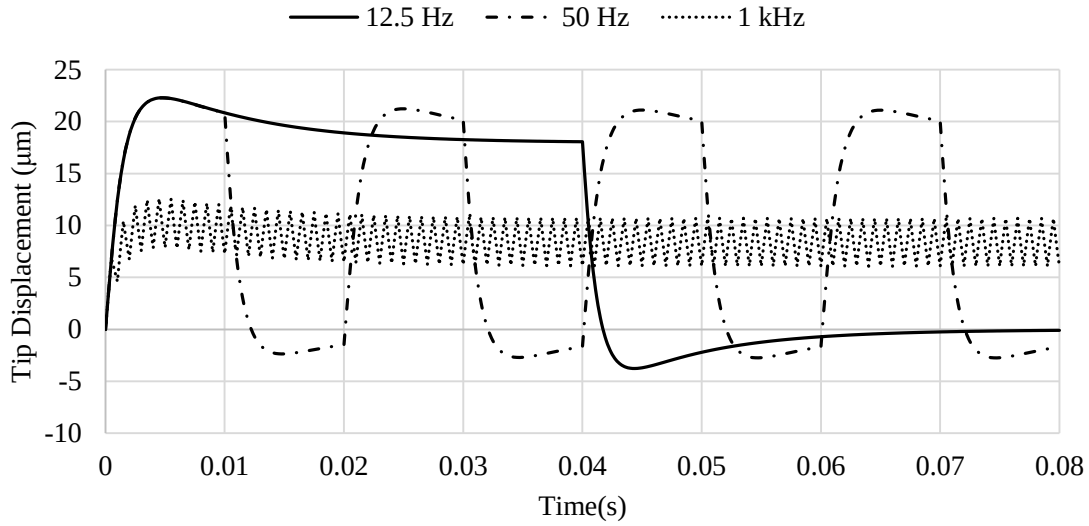

Fig. 21. Frequency response of the extension arm tip displacement, assuming a 9.6 Vpp pulse-width modulated input with 50% duty cycle.

4.6. Conclusions

A computational method has been presented that permits the calculation of the transient temperature distribution in a thermal microactuator, accounting for radiation, intra-device heat transfer, and the nonlinear temperature dependence of material properties. In the study presented, it was shown that the mechanical response of the actuator was limited by the thermal response time, permitting the thermo-mechanical problem to be treated quasi-statically. Displacement could be calculated by evaluating the time evolution of the temperature distribution and inputting it into the thermo-mechanical model.

Applying the presented model to the test actuator, the thermal time constant was estimated to be 7.25 ms, corresponding with a thermal penetration depth of approximately 400 μm. Verification of the computational method for the dynamic implementation of the microactuator model was performed by experimentally measuring the time evolution of the current drawn by the test actuator. Model predictions for the time response of the actuator show relatively good agreement with experiments, though the model predictions exhibit a slightly faster time response. This is likely due to the large temperature gradients that initially exist in the air surrounding the actuator. As heat has time to diffuse radially, the penetration depth increases, causing $h_{eq}(T)$ to decrease. The presented model does not account for the evolution of the penetration depth, and therefore predicts a slightly more rapid thermal response.

5. SUMMARY AND CONCLUSIONS

In this paper, a model has been introduced to predict the performance of thermal microactuators at high power inputs, fully considering radiation, intra-device heat transfer across an air gap, and the nonlinear temperature dependence of material properties. An electro-thermal model was first developed to predict the temperature distribution in the actuator, and a computational method was presented in which the Galerkin method with Newton-Raphson iteration was employed to solve the highly nonlinear governing heat balance equations. The temperature distribution computed using the electro-thermal model then composed the input to the thermo-mechanical model, which applied the method of virtual work to calculate the displacement of the actuator given the thermal expansion in the device.

The thermal microactuator model was first utilized to predict the steady state performance of a thermal flexure actuator, and model predictions were found to match experimental measurements very well. Sources of nonlinearity in the model were then investigated, and all but the effects of radiation were found to have a significant impact on model predictions at high power inputs. Neglecting intra-device heat transfer or the nonlinear temperature dependence of either the electrical resistivity of silicon or the thermal conductivity of air was shown to over-predict the operating temperature in the device at high power inputs. As a consequence of this over-prediction, models making the aforementioned assumptions were found to over-predict both actuator displacement and resistance. Models that assumed the thermal conductivity of silicon or the thermal expansion coefficient of silicon to be temperature-independent were shown to significantly under-predict device displacement at high power inputs. Moreover, assuming the thermal conductivity of silicon to be temperature-independent was shown to also under-predict the resistance of the actuator.

The implementation of the microactuator model was then expanded to consider the dynamic performance of the flexure actuator. The same computational method was used for the dynamic implementation as for the steady state, with the addition of an implicit Euler method that permitted the calculation of the temperature distribution after a finite time step. Using the dynamic implementation of the model, the thermal time constant for the presented flexure actuator was found to be approximately 7.25 ms. Model predictions using the dynamic implementation were then verified by measuring the current and voltage across the flexure actuator over time. The model was found to predict the electrical performance of the device relatively well, but was found to predict a slightly faster time response than was observed experimentally. This was determined to be the result of neglecting the variation in the thermal penetration depth over time.

The presented thermal microactuator model and computational method enable the prediction of thermal microactuator performance over a large range of electrical power inputs without requiring a fine mesh to produce accurate results. Implementation of the presented methodology offers MEMS designers the ability to design high performance thermal microactuators while minimizing the cost associated with design iteration. Moreover, the presented model offers improved capability for design and analysis of a wide range of heat producing micromachined devices and enables designers to better predict operating temperatures for devices used in temperature-sensitive applications.

REFERENCES

[1] R. Legtenberg, A. Groeneveld, and M. Elwenspoek, "Comb-drive actuators for large displacements," *Journal of Micromechanics and microengineering,* vol. 6, p. 320, 1996.

[2] M. P. De Boer, D. L. Luck, W. R. Ashurst, R. Maboudian, A. D. Corwin, J. A. Walraven, *et al.*, "High-performance surface-micromachined inchworm actuator," *Microelectromechanical Systems, Journal of,* vol. 13, pp. 63-74, 2004.

[3] R. Toda and E. H. Yang, "A normally latched, large-stroke, inchworm microactuator," *J. Micromech. Microeng,* vol. 17, pp. 1715-1720, 2007.

[4] A. A. Geisberger and N. Sarkar, "Techniques in MEMS microthermal actuators and their applications," in *MEMS/NEMS*, ed US: Springer, 2006, pp. 1191-1251.

[5] D. Yan, A. Khajepour, and R. Mansour, "Modeling of two-hot-arm horizontal thermal actuator," *Journal of Micromechanics and Microengineering,* vol. 13, p. 312, 2003.

[6] Z. Wang, X. Shen, and X. Chen, "Design, modeling, and characterization of a MEMS electrothermal microgripper," *Microsystem Technologies*, pp. 1-8, 2015.

[7] M. Mayyas, "Comprehensive Thermal Modeling of ElectroThermoElastic Microstructures," *Actuators,* vol. 1, pp. 21-35, 2012.

[8] S. C. Chen and M. L. Culpepper, "Design of a six-axis micro-scale nanopositioner—μHexFlex," *Precision engineering,* vol. 30, pp. 314-324, 2006.

[9] A. Atre, "Analysis of out-of-plane thermal microactuators," *Journal of micromechanics and microengineering,* vol. 16, p. 205, 2006.

[10] D. Yan, A. Khajepour, and R. Mansour, "Design and modeling of a MEMS bidirectional vertical thermal actuator," *Journal of Micromechanics and Microengineering,* vol. 14, p. 841, 2004.

[11] Q. A. Huang and N. K. S. Lee, "Analysis and design of polysilicon thermal flexure actuator," *Journal of Micromechanics and Microengineering*, vol. 9, p. 64, 1999.

[12] E. T. Enikov, S. S. Kedar, and K. V. Lazarov, "Analytical model for analysis and design of V-shaped thermal microactuators," *Microelectromechanical Systems, Journal of*, vol. 14, pp. 788-798, 2005.

[13] R. Hickey, M. Kujath, and T. Hubbard, "Heat transfer analysis and optimization of two-beam microelectromechanical thermal actuators," *Journal of Vacuum Science & Technology A*, vol. 20, pp. 971-974, 2002.

[14] J. Varona, M. Tecpoyotl-Torres, and A. A. Hamoui, "Modeling of MEMS Thermal Actuation with External Heat Source," in *Electronics, Robotics and Automotive Mechanics Conference*, 2007, pp. 591-596.

[15] C. H. Pan, C. L. Chang, and Y. K. Chen, "Design and fabrication of an electro-thermal microactuator with multidirectional in-plane motion," *Journal of Micro/Nanolithography, MEMS, and MOEMS*, vol. 4, pp. 033008-033008, 2005.

[16] S. M. Karbasi, M. Shamshirsaz, M. Naraghi, and M. Maroufi, "Optimal design analysis of electrothermally driven microactuators," *Microsystem technologies*, vol. 16, pp. 1065-1071, 2010.

[17] A. V. S. S. Prasad, K. P. Venkatesh, R. Pratap, and N. Bhat, "Improved design methodology for the development of electrically actuated MEMS structures," in *VLSI Design and 2014 13th International Conference on Embedded Systems, 2014 27th International Conference*, 2014, pp. 499-503.

[18] U. Dürig, "Fundamentals of micromechanical thermoelectric sensors," *Journal of Applied Physics*, vol. 98, p. 044906, 2005.

[19] B. Borovic, F. L. Lewis, D. Agonafer, E. S. Kolesar, M. M. Hossain, and D. O. Popa, "Method for determining a dynamical state-space model for control of thermal MEMS devices," *Microelectromechanical Systems, Journal of,* vol. 14, pp. 961-970, 2005.

[20] A. Geisberger, N. Sarkar, M. Ellis, and G. D. Skidmore, "Electrothermal properties and modeling of polysilicon microthermal actuators," *Microelectromechanical Systems, Journal of,* vol. 12, pp. 513-523, 2003.

[21] A. Atre, "Design optimization of a surface micromachined electro-thermal beam flexure polysilicon actuator," in *Proceedings of the Modeling and Simulation of Microsystems*, 2005, pp. 493-496.

[22] A. Alwan and N. R. Aluru, "Analysis of hybrid electrothermomechanical microactuators with integrated electrothermal and electrostatic actuation," *Microelectromechanical Systems, Journal of,* vol. 18, pp. 1126-1136, 2009.

[23] R. S. Chen, C. Kung, and G. B. Lee, "Analysis of the optimal dimension on the electrothermal microactuator," *Journal of Micromechanics and Microengineering,* vol. 12, p. 291, 2002.

[24] N. D. Mankame and G. K. Ananthasuresh, "Comprehensive thermal modelling and characterization of an electro-thermal-compliant microactuator.," *Journal of Micromechanics and Microengineering,* vol. 11, p. 452, 2001.

[25] R. E. Mackay, H. R. Le, and R. P. Keatch, "Design optimisation and fabrication of SU-8 based electro-thermal micro-grippers," *Journal of Micro-Nano Mechatronics,* vol. 6, pp. 13-22, 2011.

[26] X. Pu, W. Li, and Z. Zhou, "Electrothermal-driven gap adjustable MEMS comb structure: modeling and simulation of the equivalent circuit macromodel," *Microsystem Technologies,* vol. 20, pp. 1205-1212, 2014.

[27] J. V. Crosby and M. G. Guvench, "Experimentally matched finite element modeling of thermally actuated SOI MEMS micro-grippers using COMSOL multiphysics," in *Proceedings of the COMSOL Conference.*, 2009.

[28] R. W. Johnstone and M. Parameswaran, "Modelling surface-micromachined electrothermal actuators," *Electrical and Computer Engineering, Canadian Journal of,* vol. 29, pp. 193-202, 2004.

[29] R. G. Li, Q. A. Huang, and W. H. Li, "A nodal analysis method for simulating the behavior of electrothermal microactuators," *Microsystem Technologies,* vol. 14, pp. 119-129, 2008.

[30] B. Solano, S. Rolt, and D. Wood, "Thermal and mechanical analysis of an SU8 polymeric actuator using infrared thermography," *Proceedings of the Institution of Mechanical Engineers, Part C: Journal of Mechanical Engineering Science,* vol. 222, pp. 73-86, 2008.

[31] B. Lopez-Walle, M. Gauthier, and N. Chaillet, "Dynamic modelling for thermal micro-actuators using thermal networks," *International Journal of Thermal Sciences,* vol. 49, pp. 2108-2116, 2010.

[32] Y. J. Yang and C. C. Yu, "Extraction of heat-transfer macromodels for MEMS devices," *Journal of Micromechanics and Microengineering,* vol. 14, p. 587, 2004.

[33] V. A. Henneken, M. Tichem, and P. M. Sarro, "Improved thermal U-beam actuators for micro-assembly," *Sensors and Actuators A: Physical,* vol. 142, pp. 298-305, 2008.

[34] C. D. Lott, T. W. McLain, J. N. Harb, and L. L. Howell, "Modeling the thermal behavior of a surface-micromachined linear-displacement thermomechanical microactuator," *Sensors and Actuators A: Physical,* vol. 101, pp. 239-250, 2002.

[35] Y. S. Kim, N. G. Dagalakis, and S. K. Gupta, "Creating large out-of-plane displacement electrothermal motion stage by incorporating beams with step features," *Journal of Micromechanics and Microengineering*, vol. 23, p. 055008, 2013.

[36] D. O. Popa, B. H. Kang, J. T. Wen, H. E. Stephanou, G. Skidmore, and A. Geisberger, "Dynamic modeling and input shaping of thermal bimorph MEMS actuators," in *Robotics and Automation, 2003. Proceedings. ICRA'03. IEEE International Conference on*, 2003, pp. 1470-1475.

[37] L. Li and D. Uttamchandani, "Dynamic response modelling and characterization of a vertical electrothermal actuator," *Journal of Micromechanics and Microengineering*, vol. 19, p. 075014, 2009.

[38] M. S. Baker, J. A. Walraven, T. J. Headley, and R. A. Plass, "Final Report: Compliant Thermo-mechanical MEMS Actuators, LDRD# 52553," Department of Energy, United States2004.

[39] K. Miller, A. Cowen, G. Hames, and B. Hardy, "SOIMUMPs design handbook," MEMScAP Inc., Durham2004.

[40] S. M. Sze and K. K. Ng, "Physics and properties of semiconductors—A review," in *Physics of semiconductor devices*, ed, 2002, pp. 5-75.

[41] N. Ono, K. Kitamura, K. Nakajima, and Y. Shimanuki, "Measurement of Young's modulus of silicon single crystal at high temperature and its dependency on boron concentration using the flexural vibration method," *Japanese Journal of Applied Physics*, vol. 39, p. 368, 2000.

[42] A. K. Swarnakar, O. Van der Biest, and J. Vanhellemont, "Determination of the Si Young's modulus between room and melt temperature using the impulse excitation technique," *physica status solidi (c)*, vol. 11, pp. 150-155, 2014.

[43] M. Hopcroft, W. D. Nix, and T. W. Kenny, "What is the Young's Modulus of Silicon?," *Microelectromechanical Systems, Journal of,* vol. 19, pp. 229-238, 2010.

[44] A. Faghri, Y. Zhang, and J. R. Howell, *Advanced heat and mass transfer*: Global Digital Press, 2010.

[45] D. R. Lide, *CRC Handbook of Chemistry and Physics*. Boca Raton, Fla: CRC Press, 1994.

[46] P. D. Desai, "Thermodynamic properties of iron and silicon," *Journal of physical and chemical reference data,* vol. 15, pp. 967-983, 1986.

[47] Y. A. Cengel and M. A. Boles, *Thermodynamics: an engineering approach*: McGraw-Hill Education, 2015.

[48] O. Ozsun, B. E. Alaca, A. D. Yalcinkaya, M. Yilmaz, M. Zervas, and Y. Leblebici, "On heat transfer at microscale with implications for microactuator design," *Journal of Micromechanics and Microengineering,* vol. 19, p. 045020, 2009.

[49] K. G. T. Hollands, T. E. Unny, G. D. Raithby, and L. Konicek, "Free convective heat transfer across inclined air layers," *Journal of Heat Transfer,* vol. 98, pp. 189-193, 1976.

[50] M. M. Yovanovich, "A general expression for predicting conduction shape factors," *AIAA Prog. in Astro. and Aeronautics: Thermophysics and Space Craft Control,* vol. 35, pp. 265-291, 1974.

[51] S. Anand, J. Sutanto, M. S. Baker, M. Okandan, and J. Muthuswamy, "Electrothermal Microactuators With Peg Drive Improve Performance for Brain Implant Applications," *Microelectromechanical Systems, Journal of,* vol. 21, pp. 1172-1186, 2012.

[52] L. M. Phinney, D. S. Epp, M. S. Baker, J. R. Serrano, and A. D. Gorby, "Thermomechanical Measurements on Thermal Microactuators," Sandia National Laboratories, Albuquerque2009.

[53] E. B. Becker, G. F. Carey, and J. T. Oden, *Finite Elements, An Introduction: Volume I.*, 1981.

[54] C. P. Neuman and A. Sen, "Galerkin's procedure, quasilinearization, and nonlinear boundary-value problems," *Journal of Optimization Theory and Applications*, vol. 9, pp. 433-437, 1972.

[55] R. A. Sayer, E. S. Piekos, and L. M. Phinney, "Modified data analysis for thermal conductivity measurements of polycrystalline silicon microbridges using a steady state Joule heating technique," *Review of Scientific Instruments*, vol. 83, p. 124904, 2012.

[56] L. M. Phinney, J. D. Kuppers, and R. C. Clemens, "Thermal Conductivity Measurements of SUMMiT TM V Polycrystalline Silicon," Sandia National Laboratories, Albuquerque2006.

[57] K. Park, J. Lee, Z. M. Zhang, and W. P. King, "Frequency-dependent electrical and thermal response of heated atomic force microscope cantilevers," *Microelectromechanical Systems, Journal of*, vol. 16, pp. 213-222, 2007.

APPENDIX A

ELEMENT STIFFNESS MATRIX

To illustrate the derivation of the element stiffness matrix, the steady state implementation of the thermal microactuator model will be considered as an example. The element stiffness matrix can be determined by taking the derivative of the element load vector with respect to the coefficients of the shape functions, c_i.

$$K_{ij}^{e}(c^k) = \left.\frac{\partial F_i^e}{\partial c_j}\right|_{c^k} \tag{98}$$

Within the actuator, this can be written as:

$$\begin{aligned} K_{ij}^{e}(c) = &\left[-\frac{k_{0Si}}{\phi_m(\xi)c_m} A\phi_i(\xi)\frac{d\phi_j(\xi)}{d\xi}\frac{d\xi}{ds} + \frac{k_{0Si}}{[\phi_m(\xi)c_m]^2} A\phi_i(\xi)\phi_j(\xi)\right]\Bigg|_{-1}^{1} \\ &+ \int_{-1}^{1}\Bigg[\frac{k_0}{\phi_m(\xi)c_m} A\frac{d\phi_i(\xi)}{d\xi}\frac{d\xi}{ds}\frac{d\phi_j(\xi)}{d\xi}\frac{d\xi}{ds} \\ &\quad - \frac{k_0}{[\phi_m(\xi)c_m]^2} A\frac{d[\phi_m(\xi)c_m]}{d\xi}\frac{d\xi}{ds}\frac{d\phi_i(\xi)}{d\xi}\frac{d\xi}{ds}\phi_j(\xi) \\ &\quad + 4\varepsilon\sigma S_r[\phi_m(\xi)c_m]^3\phi_i(\xi)\phi_j(\xi) \\ &\quad + S_{cd}\Lambda[k_{a0} + k_{a1}\phi_m(\xi)c_m + k_{a2}[\phi_m(\xi)c_m]^2]\phi_i(\xi)\phi_j(\xi) \\ &\quad - J^2 A\phi_i(\xi)\phi_j(\xi)[\rho_1 + 2\rho_2\phi_m(\xi)c_m + 3\rho_3[\phi_m(\xi)c_m]^2 \\ &\qquad + 4\rho_4[\phi_m(\xi)c_m]^3]\Bigg]\frac{ds}{d\xi}\,d\xi \end{aligned} \tag{99}$$

Here $\Lambda = S_f/A_{cd}$.

$$K_{ij}^{e}(c) = \left[-\frac{k_{0Si}}{T(\xi)} A\phi_i(\xi) \frac{d\phi_j(\xi)}{d\xi} \frac{d\xi}{ds} + \frac{k_{0Si}}{T(\xi)^2} A\phi_i(\xi)\phi_j(\xi) \right]\Bigg|_{-1}^{1}$$

$$+ \int_{-1}^{1} \Bigg[\frac{k_0}{T(\xi)} A \frac{d\phi_i(\xi)}{d\xi} \frac{d\xi}{ds} \frac{d\phi_j(\xi)}{d\xi} \frac{d\xi}{ds}$$

$$- \frac{k_0}{T(\xi)^2} \frac{dT(\xi)}{d\xi} \frac{d\xi}{ds} A \frac{d\phi_i(\xi)}{d\xi} \frac{d\xi}{ds} \phi_j(\xi) \tag{100}$$

$$+ 4\varepsilon\sigma S_r T(\xi)^3 \phi_i(\xi)\phi_j(\xi)$$

$$+ S_{cd}\Lambda[k_{a0} + k_{a1}T(\xi) + k_{a2}T(\xi)^2]\phi_i(\xi)\phi_j(\xi)$$

$$- J^2 A\phi_i(\xi)\phi_j(\xi)[\rho_1 + 2\rho_2 T(\xi) + 3\rho_3 T(\xi)^2 + 4\rho_4 T(\xi)^3] \Bigg] \frac{ds}{d\xi}\, d\xi$$

To enforce the Neumann boundary condition at the tip of the extension arm, the first term is replaced by the following:

$$K_{pp,0}^{e} = \Lambda[k_{a0} + k_{a1}T(\xi = 1) + k_{a2}T(\xi = 1)^2]A_e. \tag{101}$$

Within the air gap, the stiffness matrix can be written as:

$$
\begin{aligned}
K_{ij}^{e}(c) = -\oint_{\partial\Omega^m} \Bigg[& [k_{a1} + 2k_{a2}\phi_m(\xi,\eta)c_m]h\left[\frac{\partial[\phi_m(\xi,\eta)c_m]}{\partial\xi}\frac{\partial\xi}{\partial n}\right. \\
& \left. + \frac{\partial[\phi_m(\xi,\eta)c_m]}{\partial\eta}\frac{\partial\eta}{\partial n}\right]\phi_i(\xi,\eta)\phi_j(\xi,\eta) \\
& + [k_{a0} + k_{a1}\phi_m(\xi,\eta)c_m \\
& + k_{a2}[\phi_m(\xi,\eta)c_m]^2]h\phi_i(\xi,\eta)\left[\frac{\partial\phi_j(\xi,\eta)}{\partial\xi}\frac{\partial\xi}{\partial n}\right. \\
& \left. + \frac{\partial\phi_j(\xi,\eta)}{\partial\eta}\frac{\partial\eta}{\partial n}\right]\Bigg] dl \\
+ \iint_{\Omega^m} \Bigg[& \big[k_{a1}\phi_j(\xi,\eta) \\
& + 2k_{a2}\phi_m(\xi,\eta)c_m\phi_j(\xi,\eta)\big]h\left[\frac{\partial[\phi_m(\xi,\eta)c_m]}{\partial\xi}\frac{d\xi}{dx}\frac{\partial\phi_i(\xi,\eta)}{\partial\xi}\frac{d\xi}{dx}\right. \\
& \left. + \frac{\partial[\phi_m(\xi,\eta)c_m]}{\partial\eta}\frac{d\eta}{dy}\frac{\partial\phi_i(\xi,\eta)}{\partial\eta}\frac{d\eta}{\partial y}\right] \\
& + [k_{a0} + k_{a1}\phi_m(\xi,\eta)c_m \\
& + k_{a2}[\phi_m(\xi,\eta)c_m]^2]h\left[\frac{\partial\phi_i(\xi,\eta)}{\partial\xi}\frac{d\xi}{dx}\frac{\partial\phi_j(\xi,\eta)}{\partial\xi}\frac{d\xi}{dx}\right. \\
& \left. + \frac{\partial\phi_i(\xi,\eta)}{\partial\eta}\frac{d\eta}{dy}\frac{\partial\phi_j(\xi,\eta)}{\partial\eta}\frac{d\eta}{dy}\right] \\
& + \Lambda S_{cd}[k_{a0} + k_{a1}\phi_m(\xi,\eta)c_m \\
& + k_{a2}[\phi_m(\xi,\eta)c_m]^2]\phi_i(\xi,\eta)\phi_j(\xi,\eta)\Bigg]\frac{dx}{d\xi}\frac{dy}{d\eta}\, d\xi\, d\eta
\end{aligned}
\tag{102}
$$

$$
\begin{aligned}
K_{ij}^{e}(c) = -\oint_{\partial\Omega^m} \Bigg[& [k_{a1} + 2k_{a2}T(\xi,\eta)]h\left[\frac{\partial T(\xi,\eta)}{\partial \xi}\frac{\partial \xi}{\partial n}\right. \\
& \left. + \frac{\partial T(\xi,\eta)}{\partial \eta}\frac{\partial \eta}{\partial n}\right]\phi_i(\xi,\eta)\phi_j(\xi,\eta) \\
& + \left[k_{a0} + k_{a1}T(\xi,\eta)\right. \\
& \left. + k_{a2}T(\xi,\eta)^2\right]h\phi_i(\xi,\eta)\left[\frac{\partial \phi_j(\xi,\eta)}{\partial \xi}\frac{\partial \xi}{\partial n}\right. \\
& \left. + \frac{\partial \phi_j(\xi,\eta)}{\partial \eta}\frac{\partial \eta}{\partial n}\right]\Bigg] dl \\
+ \iint_{\Omega^m} \Bigg[& \left[k_{a1}\phi_j(\xi,\eta)\right. \\
& \left. + 2k_{a2}T(\xi,\eta)\phi_j(\xi,\eta)\right]h\left[\frac{\partial T(\xi,\eta)}{\partial \xi}\frac{d\xi}{dx}\frac{\partial \phi_i(\xi,\eta)}{\partial \xi}\frac{d\xi}{dx}\right. \\
& \left. + \frac{\partial T(\xi,\eta)}{\partial \eta}\frac{d\eta}{dy}\frac{\partial \phi_i(\xi,\eta)}{\partial \eta}\frac{d\eta}{\partial y}\right] + \left[k_{a0} + k_{a1}T(\xi,\eta)\right. \\
& \left. + k_{a2}T(\xi,\eta)^2\right]h\left[\frac{\partial \phi_i(\xi,\eta)}{\partial \xi}\frac{d\xi}{dx}\frac{\partial \phi_j(\xi,\eta)}{\partial \xi}\frac{d\xi}{dx}\right. \\
& \left. + \frac{\partial \phi_i(\xi,\eta)}{\partial \eta}\frac{d\eta}{dy}\frac{\partial \phi_j(\xi,\eta)}{\partial \eta}\frac{d\eta}{dy}\right] \\
& + \Lambda S_{cd}\left[k_{a0} + k_{a1}T(\xi,\eta)\right. \\
& \left. + k_{a2}T(\xi,\eta)^2\right]\phi_i(\xi,\eta)\phi_j(\xi,\eta)\Bigg]\frac{dx}{d\xi}\frac{dy}{d\eta}\, d\xi\, d\eta.
\end{aligned}
\tag{103}
$$

The global stiffness matrix can then be assembled using (59).